AMERICAN UNIVERSITY OF BEIRUT

OPTIMIZED DESIGN OF A BARBED SUTURE FOR FLEXOR TENDON REPAIR UNDER FATIGUE LOADING: EXPERIMENTALLY INFORMED EXTENDED FINITE ELEMENT ANALYSIS

by

HADEEL KASSEM HIJAZI

A thesis
submitted in partial fulfillment of the requirements
for the degree of Master of Engineering
to the Department of Mechanical Engineering
of the Faculty of Engineering and Architecture
at the American University of Beirut

Beirut, Lebanon
April 2017

AMERICAN UNIVERSITY OF BEIRUT

OPTIMIZED DESIGN OF A BARBED SUTURE FOR FLEXOR TENDON REPAIR UNDER FATIGUE LOADING: EXPERIMENTALLY INFORMED EXTENDED FINITE ELEMENT ANALYSIS

by

HADEEL K. HIJAZI

Approved by:

Dr. Elie Shammas, Assistant Professor — Advisor
Mechanical Engineering

Dr. Mu'Tasem Shehadeh, Associate Professor — Member of Committee
Mechanical Engineering

Dr. Youssef Bakhach, Assistant Professor — Member of Committee
Surgery

Date of thesis defense: April 27, 2017

AMERICAN UNIVERSITY OF BEIRUT

THESIS, DISSERTATION, PROJECT RELEASE FORM

Student Name:
_____

Last First Middle

◯ Master's Thesis ◯ Master's Project ◯ Doctoral Dissertation

☐ I authorize the American University of Beirut to: (a) reproduce hard or electronic copies of my thesis, dissertation, or project; (b) include such copies in the archives and digital repositories of the University; and (c) make freely available such copies to third parties for research or educational purposes.

☐ I authorize the American University of Beirut, to: (a) reproduce hard or electronic copies of it; (b) include such copies in the archives and digital repositories of the University; and (c) make freely available such copies to third parties for research or educational purposes

after:

One ---- year from the date of submission of my thesis, dissertation, or project.
Two ---- years from the date of submission of my thesis, dissertation, or project.
Three ---- years from the date of submission of my thesis, dissertation, or project.

_____

Signature Date

ACKNOWLEDGMENTS

I would like to thank my advisors, Dr. Elie Shammas and Dr. Mu'Tasem Shehadeh, for their continuous support and guidance throughout my thesis. Working with them was the best part of my journey at AUB.

Special thanks to Dr. Youssef Bakhach for his valuable medical guidance.

I would also like to thank Dr. Mohammad Ghassan Abiad for allowing me to use the experimental setup that is capable to get the material properties.

I would like to dedicate my work to the soul of my brother, Ali, who had always believed in me. I hope that today I made him proud!

AN ABSTRACT OF THE THESIS OF

Hadeel K. Hijazi for Master of Engineering

Major: Mechanical Engineering

Title: Optimized Design of a Barbed Suture for Flexor Tendon Repair under Fatigue Loading: Experimentally Informed Extended Finite Element Analysis

Flexor tendons are essential for hand function. Surgeries for these tendons are very serious and challenging; the repair site must endure active and passive immobilization forces in an arrangement that would guarantee the integrity of the tendon to redevelop. Early active mobilization is considered in some rehabilitation programs. This type of motion prevents tissue adhesion and results in a faster healing process. Hence, tendons must sustain forces under cyclic loading conditions. The conventional surgical technique requires tying some knots at the end of the tendon repaired site; these knots have many drawbacks that affect the tendon performance. Recently, barbed sutures are introduced to ensure the same security and strength as conventional sutures while decreasing tissue distortion and uniformly holding the forces. Previous work considered suturing with multiple strands; some work studied the validity of using a single suture but was restricted to the analysis of stresses under static loading conditions in order to attain the best suture configuration.

The objective of this study is to comprehend the effect of the geometric change of the suture on its strength and to design a single suture that will tolerate the tendon force under cyclic loading. Four different elliptical aspect ratios (ratio of major to minor axis = $\rho = 1/2, 1, 2, 3$) suitable with the tendon's geometry, were considered to study the strength of the suture and that of the barb.

Using the extended finite element analysis in Abaqus, two loading conditions were applied on each aspect ratio, ρ, to acquire the one with the highest strength. Paris Law that uses the principles of linear elastic fracture mechanics was implemented to model the sutures under fatigue loading. Barbed suture with $\rho = 2$ was optimized for two cut angles (154°, 160°) and three cut depths (0.07mm, 0.12mm, 0.18mm) under a third loading condition that represents the suture-tendon interaction. Results show that the best design for a barbed suture under fatigue loading has an aspect ratio 2 with a cut angle of 154° and cut depth 0.19 mm.

CONTENTS

ACKNOWLEDGMENTS v

ABSTRACT vi

ILLUSTRATIONS ix

TABLES xi

Chapter

1. INTRODUCTION 1

1.1. Objective 3

2. THEORETICAL BACKGROUND 5

2.1. Viscoelasticity 5

2.2. Fracture Mechanics 7

3. METHODOLOGY 11

3.1. Experiments 11

3.1.1. Tensile Test 12
3.1.2. Stress Relaxation Test 14
3.1.3. Fatigue Test 14

3.2. Finite Element Analysis [28] 15

3.2.1. Determination of Viscoelastic Material Parameters 15
3.2.2. Extended Finite Element Method 16
3.2.3. Direct Cyclic Approach 17

4. MODELING WITH ABAQUS 21

4.1. Geometry 21

4.2. Material 26

4.3. Step [28] 30

4.4. Interaction 34

4.5. Boundary Conditions and Loading 37

4.5.1. Suture Strength 38
4.5.2. Barb Strength 39
4.5.3. Tendon-Suture Interaction 41

4.6. Mesh 43

4.6.1. Load case 1 43
4.6.2. Load case 2 46

5. RESULTS 47

5.1. Suture Strength 47

5.2. Barb Strength 49

5.3. Optimization 51

6. DISCUSSION OF RESULTS 54

7. CONCLUSION AND FUTURE WORK 58

7.1. Conclusion 58

7.2. Future Work 58

REFERENCES 59

ILLUSTRATIONS

Figure Page

1. A – Modified Kessler, B – Double modified Kessler, C – 4-strand Savage and D – 6-strand Savage [6] 1
2. Generalized crack growth rate versus strain energy release rate [26] 10
3. UTM machine and anchoring mechanism 12
4. Elastic stiffness degradation as a function of the cycle number [28] 18
5. Paris Regime for Fatigue Crack Growth [28] 19
6. Suture's parameters representation [14] 21
7. Major axis (a), minor axis (b) and cut depth of an ellipse 22
8. $\rho = ½$ 24
9. $\rho = 1$ 25
10. $\rho = 2$ 25
11. $\rho = 3$ 25
12. Curve fit of stress relaxation data 27
13. Stress-Strain curve 28
14. Polypropylene stress intensities for Modes I and II [40] 29
15. Stabilization of Fourier coefficients [28] 31
16. FCP of polyethylene [36] 35
17. Suture strength 39
18. Barb strength 40
19. Tendon-suture interaction 43
20. Tetrahedral mesh 44

21. Mesh sensitivity for tetrahedral elements 44
22. Hexahedral structured mesh near the crack tip 45
23. Mesh convergence of structured elements 45
24. Results of Load Case 1 - Number of cycles for crack Initiation & failure 48
25. Suture strength failure mechanism 49
26. Barb strength failure mechanism 50
27. Geometry of the optimized design of a barbed suture 53
28. Crack size for $\rho = 1/2$ 54
29. Crack size for ρ = 1 55
30. Crack size for ρ = 2 55
31. Crack size for ρ = 3 56

TABLES

Table Page

1. Cross sectional areas of flexor tendons 22
2. Dimensions of minor axes and aspect ratios of flexor tendons 23
3. Equivalent cut depths, major and minor axes for different aspect ratios 24
4. Modes I, II, and III fracture energy 29
5. Direct cyclic step parameters 34
6. VCCT fracture criterion 35
7. Amplitude definition 38
8. Mesh convergence of force-controlled model 46
9. Results of Load Case 1 - Crack initiation 47
10. Results of Load Case 2 50
11. Ellipse equivalence for the optimized geometry 51
12. Results for the optimized configurations 52

CHAPTER 1

INTRODUCTION

Flexor tendons are crucial to hand function and play an important role in power control. Fibrous rings that keep them close to the bones and enables the effective movement of joints connect these tendons. Injuries occur frequently in lacerations of the fingers, palm, or forearm. Hence, surgical suturing is a technique used to attach body tissues after an injury [1]. Recent studies consider five different techniques for suturing; modified Kessler (3-0), double modified Kessler (3-0), 4-strand Savage (3-0), 4-strand Savage (4-0), and 6-strand Savage (4-0) (Fig.1) [2-5].

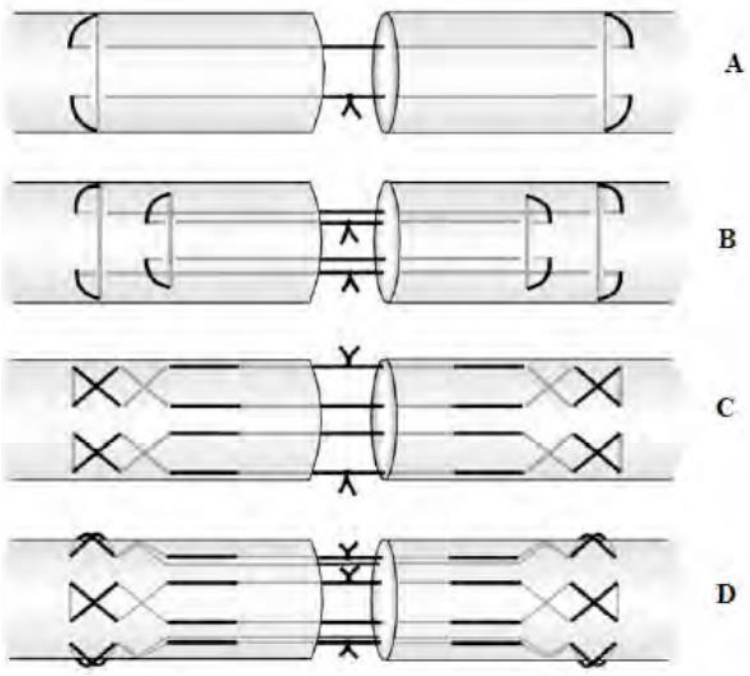

Figure 1 - A – Modified Kessler, B – Double modified Kessler, C – 4-strand Savage and D – 6-strand Savage [6]

There are two types of body sutures; biodegradable and non-biodegradable. Biodegradable sutures are those that break inside the body and do not require a second surgery to be removed. However, non-biodegradable ones need to be removed after the wound is healed [7-10].

The conventional way to lock a suture is by tying a knot at the extremities. A knot distributes the tissue holding forces along the length of the suture. This can be done by stitching, where the length of the suture can be varied between the knots. However, suture knots carry some disadvantages; it may delay the healing of a wound, restrict blood flow and cause tissue distortion. For, the security of a knot is a measure of the clinical performance of a suture [2, 4, 11, 12].

Knots are considered to be weak points in tendon repair and rupture upon increasing tension [13]. The material needed for tendon repair must be strong enough to withstand the tension. In recent years, knotless sutures have been developed in a way that gives the same security as conventional ones [14]. Barbed sutures were introduced first by McKenzie and Bunnell for tendon repair [15]. It is believed that this type of sutures is advantageous over conventional ones. It has the ability to reduce suture slippage in the wound due to tension produced in the tissue [11]. Barbed sutures provide high suture-tissue interaction as the barbs lock inside the tendon [5]. For easy passage, the suture enters the tendon in the opposite direction of the splay of the barb. Therefore, the barb of the suture holds the tendon in place when an opposing force is applied [2]. Yet, it decreases the tissue distortion by uniformly distributing the holding forces [16, 17].

Finite element analysis is a method that enables the study of stress flow patterns, displacement patterns and interactions between two materials in contact. Earlier investigations were made to study the effect of different barbed geometries on the displacement of the barb under loading. Moreover, simulations on a single barb suture/tissue pullout test were made on different barb geometries when bounded either by skin or tendon [18]. Knowing that the tendon is stiffer than skin, the barb should be rigid to penetrate and anchor the surrounding tissue.

Ingle et al. focused on studying different arrangements of barbs with the aim of optimizing the cut angle and cut depth [11, 14, 18, 19]. In his study, the optimized cut angle and cut depth were found to be 150° and 0.18 mm respectively. If the skin is softer, the barb must be flexible to give the best skin tissue anchoring. So, a cut angle of 170° and cut depth of 0.18 mm were recommended [13]. In addition to that, the pullout force required for a barbed suture was found to be much higher than that for the unbarbed one. The suture/tissue pullout test was successful in verifying the superior capability of barbed sutures [11]. Lastly, the optimal barb design may not be the same for all surgical applications and the geometric configuration of barbs may need to be changed for different types of tissues like skin, tendon and fatty tissue [14].

1.1. Objective

Two primary objectives are considered in this study. The first is to comprehend the effect of the geometric change of the suture on its strength under fatigue loading. The other objective is to design a suture that will tolerate the tendon force for the same loading condition.

Finite element analysis made on sutures was limited on studying the stress analysis under static loading. No further investigations were made on cyclic loading conditions, and studies did not include the fracture mechanics of barbed sutures used for flexor tendon repair.

In this paper, the viscoelastic material properties of polypropylene suture is determined experimentally. Moreover, the effect of varying the cross sectional configuration, cut angle and cut depth on the strength of the suture is investigated using the extended finite element analysis in Abaqus. This method is used to predict the crack propagation of the suture under cyclic loading. Finally, the possibility of using a single barbed suture for tendon repair is assessed.

CHAPTER 2

THEORETICAL BACKGROUND

2.1. Viscoelasticity

Sutures are viscoelastic materials that exhibit viscoelastic properties and response. Creep and stress relaxation are the two commonly perceived viscoelastic behaviors [20, 21]. On one hand, creep is the time dependent variation of strain subjected to instantaneous stress. This is depicted in terms of a time dependent creep compliance, $J(t)$.

$$J(t) = \frac{\epsilon(t)}{\sigma} \qquad eq.1$$

On the other hand, stress relaxation is the time dependent change of stress in terms of an instantaneous strain. This behavior is depicted by a time dependent stress relaxation modulus, $G(t)$.

$$G(t) = \frac{\sigma(t)}{\epsilon} \qquad eq.2$$

To compute the stress-strain behavior of a viscoelastic solid subjected to an arbitrary loading, Boltzmann suggested the use of superposition principle. He assumed that creep at any time is a function of the whole previous loading history and there is an independent contribution to deformation from each loading step. Therefore, the strain under an applied stress, $\sigma(t)$, is given by:

$$\epsilon(t) = \int_{-\infty}^{t} J(t-\tau)d\sigma(t) \qquad eq.3$$

Similarly, the stress for an applied strain, $\epsilon(t)$ is given by:

$$\sigma(t) = \int_{-\infty}^{t} G(t-\tau)d\epsilon(t) \qquad eq.4$$

Viscoelastic behavior can be modelled from a linear combination of elastic and viscous performance. Elastic behavior is represented by a Hookean spring while viscous one is represented by a Newtonian dashpot. The model proposed by Voigt considers a parallel arrangement of the spring and dashpot so that the same strain applies to both elements under loading. The constitutive response is:

$$\sigma = E_V\epsilon + \eta_V\frac{d\epsilon}{dt} \qquad eq.5$$

Where $\epsilon = \frac{\sigma}{E_V}\left[1 - \exp\left(-\frac{t}{\tau'}\right)\right]$, E_V is the spring constant, η_V is the oil viscosity in the dashpot, and τ' is the retardation time.

Alternatively, Maxwell model considers a series arrangement of the spring and dashpot where both elements experience the same stress. For stress relaxation, $\frac{d\epsilon}{dt} = 0$, the constitutive model is:

$$\frac{1}{E_M}\frac{d\sigma}{dt} + \frac{\sigma}{\eta_M} = 0 \qquad eq.6$$

Where $\sigma = \sigma_0 \exp\left(-\frac{t}{\tau}\right)$, E_M is the spring constant, η_M is the oil viscosity in the dashpot, σ_0 is the initial stress, and τ' is the relaxation time.

Voigt's model is noble but cannot fully describe the stress relaxation in strained viscoelastic material. Therefore, it is a demonstration of the linear behavior subjected to creep. Likewise, Maxwell cannot account for some important aspects of

Voigt's model and accordingly represents viscoelasticity subjected to stress relaxation. Both models are illustrated by a finite series of exponentially decaying elements. Prony series in the form of $\sum_{i=1}^{N} \alpha_i . e^{-t/\tau_i}$ is one of the mathematical methods applied for the linear viscoelastic behavior.

When the behavior is depicted by Maxwell model, stress relaxation response is represented with a prony series in the form of [21, 22]:

$$E(t) = E_\infty + \sum_{i=1}^{N} E_i . e^{-t/\tau_i} \qquad eq.7$$

Where E_∞ is the long-term elastic modulus, E_i are the stress-relaxation elastic moduli associated with relaxation times τ_i related to each Prony component by the viscosities of the dashpots, and $\tau_i = \frac{\eta_i}{E_i}$.

2.2. Fracture Mechanics

Fracture mechanics study the failure of structures at a load below that necessary to cause general yielding. It is the applied mechanics used to study cracks for an existing flaw. Linear elastic fracture mechanics, LEFM, study the conditions at which an existing crack will extend by means of the crack elastic stress analysis. This approach is associated with three modes of crack surface displacement. Mode I describes the opening of a crack plane due to tensile stresses which are induced by displacements perpendicular to the plane. Mode II refers to the sliding mode caused by displacements perpendicular to the crack tip edge from in-plane shear stresses. Lastly,

mode III describes the tearing mode produced by displacements parallel to the crack tip edge from out-of-plane shear stresses [23].

Boundaries adjacent to the crack tip are stress free surfaces, and therefore stresses are distributed in the area near the crack tip. According to the three modes of failure, the stress intensity field, K, can be divided into the corresponding three basic modes of crack surface displacement ($K_I, K_{II}\ and\ K_{III}$) [24]. The following relation defines the stress intensity factor:

$$K = \sigma_a Y\sqrt{\pi c} \qquad eq.8$$

Where σ_a is the externally applied stress, Y is a geometry factor, and c is the crack half length. Knowing that Y and c are constants, the stress intensity field therefore depends on the external applied stress and on the square root of the crack length.

To avoid calculating the stresses at the crack tip, the strain energy release rate, G, can be used instead. It should be noted that K and G are analogous and using one over the other gives the same results. When the stress intensity reaches its critical value, K_C, then G_C becomes the critical energy release rate instead which leads to crack propagation and perhaps fracture. The relationship between K and G is given by:

$$G = \frac{K^2}{E} \qquad eq.9$$

The above equation is significant and used for plane stress conditions. It should be noted that for plane strain conditions, the equation becomes as such:

$$G = \frac{K^2(1-\vartheta)}{E} \qquad eq.10$$

Where E is the elastic modulus and ϑ is Poisson's ratio.

Fatigue mechanism uses the concept of stress intensity factor discussed earlier, and therefore LEFM provides an appropriate means of correlating fatigue crack growth data. Assuming an already existing crack, fatigue crack propagation using LEFM is based on Paris law that relates the rate of crack growth, $\frac{da}{dN}$, to the stress intensity factor range, ΔK. The fatigue cycle is usually represented by ΔK which is the difference between the maximum and minimum value of the stress intensity during a fatigue cycle. The basic form of Paris law is given by [23, 25-27]:

$$\frac{da}{dN} = C\Delta \mathrm{K}^n \qquad eq.11$$

The crack length and number of cycles are denoted by a and N respectively. C and n are fitting parameters that can be deduced from the Paris regime curve (Fig.2).

As stated earlier, and depicted by Irwin and Sih et al., the stress intensity factor and energy release rate are equivalent. Therefore, Paris law can be rewritten using ΔG instead of ΔK in the form of:

$$\frac{da}{dN} = Cf(G)^n = C\Delta G^n \qquad eq.12$$

Thus, crack growth modelling using fracture mechanics based on Paris law can be studied using strain energy release rate relation.

Figure 2 shows that Paris regime is bounded by two regions. At low critical energy release rates, region I is defined. The crack starts to propagate at the threshold energy release rate. Paris regime is represented in Region II where the behavior is a log-

linear one. At high energy release rates, region III shows an unstable crack growth [25, 28-31].

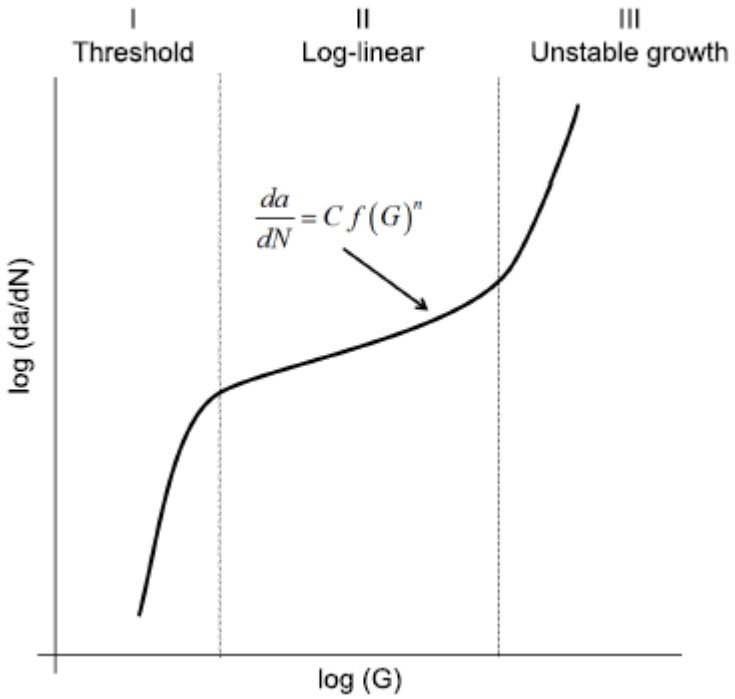

Figure 2 - Generalized crack growth rate versus strain energy release rate [26]

Linear Elastic Fracture Mechanics has been used to study the fracture characteristics of many materials and has been used to study the fracture and fatigue properties of some viscoelastic polymers [32]. Therefore, Paris model is used to study the crack propagation for the suture material used for tendon repair under cyclic loading [24, 33-35].

CHAPTER 3

METHODOLOGY

3.1. Experiments

In order to acquire the mechanical properties of sutures, a universal tensile testing machine LS1 from Lloyd Instruments was used. This machine has the ability to undergo multiple test types for different materials. NEXYGEN Plus is the software that enables the user to specify the test type, control its input and visualize the needed outputs.

Polypropylene 1 suture is the material experimented in this paper. This suture is of viscoelastic nature. Therefore, tensile and stress relaxation tests were performed in order to acquire the elastic and viscoelastic material properties respectively. An anchoring mechanism that holds the suture to the grips of the machine was designed due the slippage between the suture and the grips (Fig.3).

Polyethylene and polypropylene have similar behaviors. Results of fatigue crack propagation experiments conducted on polyethylene are used to obtain the fatigue fitting parameters needed for the direct cyclic analysis in Abaqus.

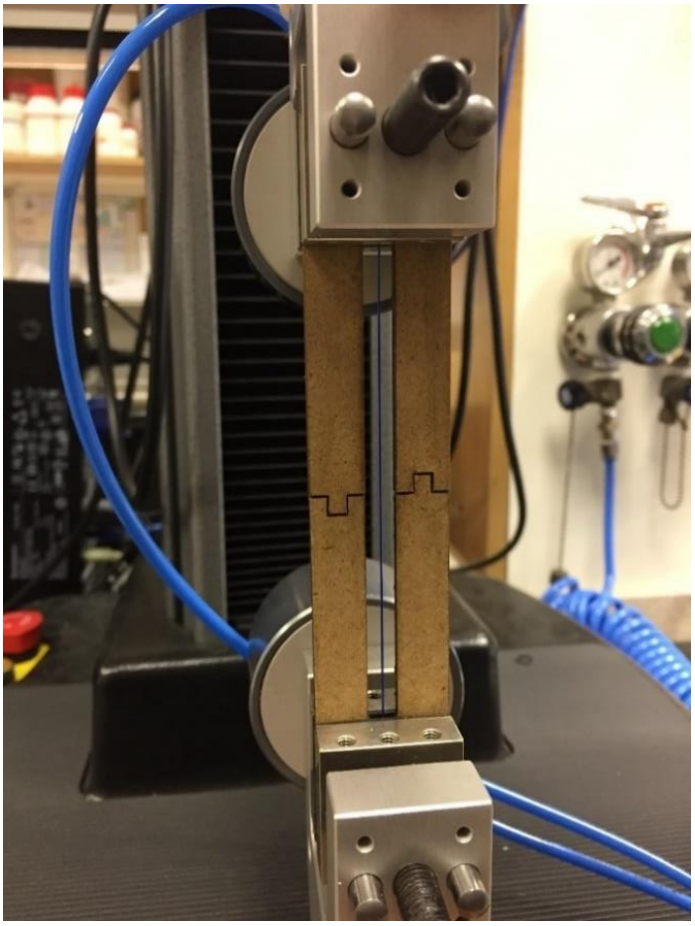

Figure 3 - UTM machine and anchoring mechanism

3.1.1. Tensile Test

A uniaxial tensile test was applied on the suture in order to obtain its modulus of elasticity, E, poisson's ratio, ϑ, and its tensile strength. The strength of the suture was acquired from the stress strain curve generated. The strain rate and the gauge length were set to 25 mm/min and 10 cm respectively, and the magnitude of the load cell used was 10 kN. The average nominal diameter of all suture samples used was 0.4 mm.

E is determined by Hooke's law given by the following equation:

$$E = \frac{\sigma}{\epsilon_x} \qquad eq.13$$

σ is the engineering stress given by:

$$\sigma = \frac{F}{A_0} \qquad eq.14$$

F is the load recorded at each instant and A_0 is the initial area of the suture. A micrometer at the beginning of the experiment measures the initial diameter of the suture.

ϵ_x is the longitudinal strain given by:

$$\epsilon_x = \frac{\Delta l}{l_0} \qquad eq.15$$

Such that Δl is the change in gauge length of the specimen with time and l_0 is the initial defined gauge length. This is attained from the curve of elongation versus time.

In order to attain the second property, ϑ, the lateral strain is required. This strain is related to the change in the diameter of the suture, Δd, with time. The initial diameter, d_0, and Δd are measured by a micrometer since it cannot be done by the uniaxial testing machine.

Poisson's ratio is represented by the following equation:

$$\vartheta = -\frac{\epsilon_y}{\epsilon_x} \qquad eq.16$$

Where ϵ_y is the lateral strain given by:

$$\epsilon_y = \frac{\Delta d}{d_0} \qquad eq.17$$

3.1.2. Stress Relaxation Test

Stress relaxation is the change in stress with time for a constant strain. In order to get the viscoelastic mechanical properties of polypropylene sutures, this test was applied on the samples to attain shear relaxation data. The UTM machine described earlier is capable of performing this test. An instantaneous strain of 0.1 mm/mm was held constant for 60 minutes for each sample. The shear test data was extracted and implemented in Abaqus to generate a fit for the stress relaxation curve and prony series coefficients.

3.1.3. Fatigue Test

ASTM E647 "Standard Test Method for Measurement of Fatigue Crack Growth Rates" measures the fatigue crack growth for metals. This method has been adopted to polymers many years ago and is therefore used to measure the crack growth rate [34,36,37]. In this test, a plot of the crack length rate, which is the change in crack length (da) for each corresponding tensile fatigue cycle (dN), versus the stress intensity factor (ΔK) is generated. The curve obtained must have a similar behavior to the log-linear region depicted earlier.

Specimens are tested with a sinusoidal waveform, frequency of 3 Hz and an R-ratio of 0.1 [36]. The test specimen has two digital cameras on both sides to screen the crack growth length. The camera records the images of the crack through the test cycle as a function of number of cycles. This number is recorded for each crack growth and specimens are cycled until fracture. The secant method is used to calculate the crack

growth rate. This includes calculating the slope of the line that connects two points according to equation 18:

$$\frac{da}{dN} = \frac{(a_{i+1} - a_i)}{(N_{i+1} - N_i)} \qquad eq.18$$

Such that a is the crack length and N is the number of cycles.

The cyclic stress intensity is calculated according to an equation that relates the load range, width and thickness of the specimen, and the geometric correction factor for compact tension specimen.

Paris law parameters, C and n, are obtained from the linear regression of region II curve. C represents the y-intercept and n the slope of this line on a log-log scale as shown in the following equation:

$$\log\left(\frac{da}{dN}\right) = \log(C) + n.\log(\Delta K) \qquad eq.19$$

3.2. Finite Element Analysis [28]

3.2.1. Determination of Viscoelastic Material Parameters

Relaxation parameters obtained from experiments are presented in four different ways in Abaqus. The user may either specify the coefficients of prony series directly, or the creep test data, or the relaxation test data, or the frequency dependent data obtained from experiments. This study focuses on the implementation of the shear test data.

The shear test data is the records of stress change with time. The stress at each instant acquired from experiments must be normalized. The data extracted is directly implemented in the data lines of the shear relaxation data of the material property.

3.2.2. Extended Finite Element Method

Modeling discontinuities, such as cracks, with finite element analysis requires the conformity of the mesh with geometric discontinuities. The extended finite element method (XFEM) was first introduced by Belytschko and Black (1999). It is an extension of the conventional finite element method based on the concept of partition of unity. It allows the presence of discontinuities in an element by enriching degrees of freedom with special displacement functions. As such, the mesh is not required to match the geometry of the discontinuities. Hence, the crack propagates along a solution-dependent path without the need to remesh the bulk material. Most importantly, XFEM allows for both material and geometrical nonlinearities; thus, it is applicable for the case of viscoelastic material.

The displacement vector, u, with the partition of unity enrichment is given by:

$$u = \sum_{I=1}^{N} N_I(x) \left[u_I + H(x) a_I + \sum_{\alpha=1}^{4} F_\alpha(x) b_I^\alpha \right] \qquad eq.20$$

Where $N_I(x)$ are the nodal shape functions, u_I is the nodal displacement vector associated with the continuous part of the finite element solution, a_I is the nodal enriched degree of freedom vector, $H(x)$ is the discontinuous jump function across

crack surfaces, b_I^{α} is the nodal enriched degree of freedom vector, and $F_{\alpha}(x)$ is the elastic asymptotic crack tip functions.

The principles of linear elastic fracture mechanics (LEFM) are used to model moving cracks in the framework of XFEM. These principles are used by the virtual crack closure technique (VCCT) that is based on the assumption that the strain energy released when a crack is extended by a certain amount equals the energy required to close the crack by the same amount. The fracture criterion involving the three modes is given by:

$$f = \frac{G_{equiv}}{G_{equivC}} \geq 1 \qquad eq.21$$

Where G_{equiv},is the equivalent strain energy release rate calculated at a node, and G_{equivC} is the critical equivalent strain energy release rate calculated by power law. The crack-tip node will debond when the fracture criterion reaches the value of 1.

Wu (1965) defined the power law by the following equation:

$$\frac{G_{equiv}}{G_{equivC}} = \left(\frac{G_I}{G_{IC}}\right)^{a_m} + \left(\frac{G_{II}}{G_{IIC}}\right)^{a_n} + \left(\frac{G_{III}}{G_{IIIC}}\right)^{a_0} \qquad eq.22$$

$G_{IC}, G_{IIC}, G_{IIIC}$, are the critical energy release rates for modes I, II, and III respectively. And a_m, a_n, a_o are the corresponding powers for each mode.

3.2.3. Direct Cyclic Approach

Establishing the load versus the number of cycles to failure (S-N) curve is one of the traditional approaches for determining the fatigue limit. As a solution for the

expensive computational costs of the damage simulations over many load cycles, some simple numerical studies for the fatigue life of structures that include modeling its response while subjected to a small fraction of the actual loading history were considered. However, such methods do not account for the development of the crack. Another approach is to apply a crack/damage evolution law that is capable for predicting the relation between the crack length and number of cycles to failure.

The direct cyclic analysis in Abaqus affords a computationally modeling technique that gives a stabilized response of an assembly subjected to periodic loading. The direct cyclic low-cycle fatigue behavior is illustrated as discrete points along the loading history.

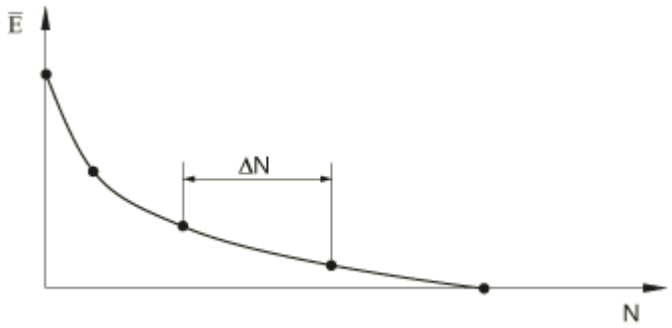

Figure 4 - Elastic stiffness degradation as a function of the cycle number [28]

The degradation and evolution of the material properties in the next increment of load cycles, ΔN, are determined by the solution at each point. Then the degraded properties are used to compute the next point solution in the load history. By that, the progressive damage and failure at the material interface and its bulk can be modelled. The onset and delamination growth at the crack tip in the interface elements are described by Paris law that relates the relative fracture energy release rate to the crack

growth rate as explained earlier. The energy release rates are calculated based on the above mentioned VCCT criterion.

The plot below (Fig.5) shows that Paris regime is bounded by a lower and upper limit. The energy release rate threshold, G_{thresh}, is the lower limit where the crack starts to propagate. Below this limit, region I, the crack is inactive and no propagation is considered. Region II, Paris regime, defines a linear crack propagation based on the power law. When the energy release rate reaches the upper limit, G_{pl}, the crack will grow at an accelerated and unstable rate. So, this defines region III where fracture of the system occurs.

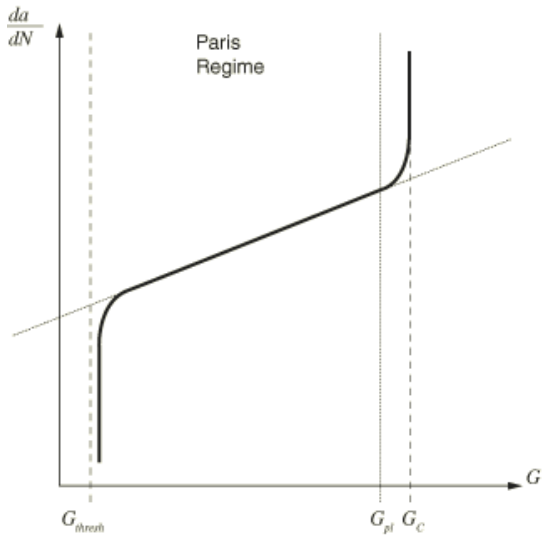

Figure 5 - Paris Regime for Fatigue Crack Growth [28]

Once the crack is initiated, the propagation rate, $\frac{da}{dN}$, is obtained from ΔG, which is the relative fracture energy release rate when the structure is loaded between its maximum and minimum values. The crack will propagate as long as the maximum

energy release rate, G_{max}, which corresponds to the cyclic energy release rate when the load is at its maximum value, is greater than G_{thresh}.

When $G_{thresh} < G_{max} < G_{pl}$ is satisfied, $\frac{da}{dN}$ can be obtained from Paris law that is given by:

$$\frac{da}{dN} = c_3 \Delta G^{c_4} \qquad eq.23$$

Where c_3 and c_4 are material constants.

CHAPTER 4

MODELING WITH ABAQUS

4.1. Geometry

To simplify the analysis, the suture was modelled as a cylinder of length 1 mm. A single barb representing the crack was sketched on the suture as a partition. The approximate distance from the crack tip to the edge is 0.4 mm.

Commercial sutures are available as circular geometries with an average nominal diameter of 0.6 mm. The cut angle, θ, and cut depth, Cd, of these sutures is 154° and 0.19 mm respectively.

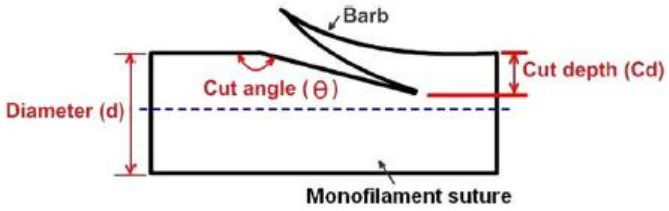

Figure 6 - Suture's parameters representation [14]

Flexor tendons have non-circular cross sectional areas. The width of flexor digitorum superficialis (FDS) and flexor digitorum profundus (FDP) for every finger along with the cross sectional areas, CA, are tabulated below [38, 39].

	Finger			
	2	**3**	**4**	**5**
FDS width	5 mm	6.5 mm	5.5 mm	3 mm
FDP width	5 mm	6 mm	5 mm	4.5 mm
FDS CA	8.36 mm^2	11.54 mm^2	10.46 mm^2	4.04 mm^2
FDP CA	11.4 mm^2	14.44 mm^2	13.42 mm^2	8.84 mm^2

Table 1 - Cross sectional areas of flexor tendons

The area of the ellipse shown (Fig.7) is given by:

$$CA = \pi ab \qquad eq.24$$

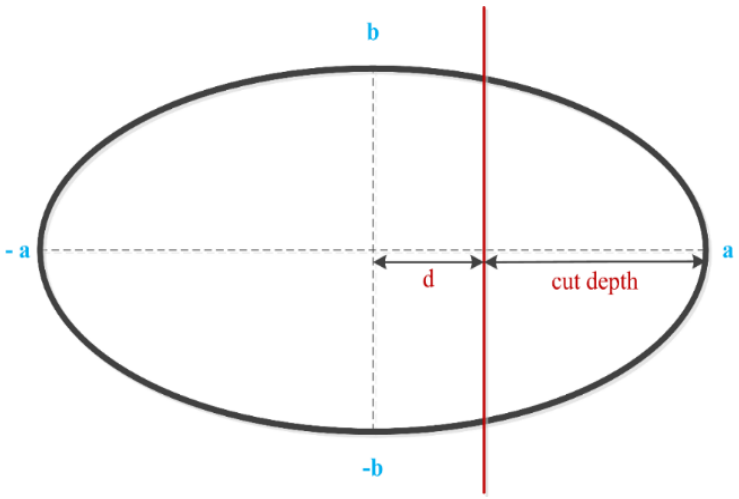

Figure 7 – Major axis (a), minor axis (b) and cut depth of an ellipse

And

$$a = \frac{finger\ width}{2} \qquad eq.25$$

Hence, the table below shows the calculated values of b and aspect ratios, $\rho = \frac{a}{b}$ (ratio of major to minor axis), of all finger tendons:

	Finger							
	2		3		4		5	
	b (mm)	**ρ**	**b (mm)**	**ρ**	**b (mm)**	**ρ**	**b (mm)**	**ρ**
FDS	1.0644	2.35	1.13	2.88	1.21	2.27	0.858	1.75
FDP	1.452	1.722	1.532	1.96	1.708	1.46	1.25	1.8

Table 2 - Dimensions of minor axes and aspect ratios of flexor tendons

Inspired by the tendon elliptical cross sectional areaa, the aspect ratios considered for modelling were $\frac{1}{2}$, 1, 2 and 3. All geometries have the same cut angle, 154°, and equivalent cut depths to 0.19 mm.

The equivalent dimensions of the major and minor axes were obtained from equations 26 and 27:

$$\pi r^2 = \pi ab \qquad eq.26$$

$$\rho = \frac{a}{b} \qquad eq.27$$

Then, the cut distance, d, of the ellipse was achieved from the below equation [6]:

$$(RA)_{ellipse} = a \times b \left(\frac{\pi}{2} + \sin^{-1}(\frac{d}{a})\right) + \frac{b \times d \times \sqrt{a^2 - d^2}}{a} \qquad eq.28$$

Such that,

$$RA_{circle} = RA_{ellipse} \qquad eq.29$$

Finally, the equivalent cut depth for each aspect ratio was obtained from equation 30 and its value along with the major and minor axes are tabulated below:

$$cut\ depth = d - a \qquad eq.30$$

	$\boldsymbol{\rho = \frac{1}{2}}$	$\boldsymbol{\rho = 1}$	$\boldsymbol{\rho = 2}$	$\boldsymbol{\rho = 3}$
a (mm)	0.2121	0.3	0.4243	0.5196
b (mm)	0.4243	0.3	0.2121	0.1732
d (mm)	0.0778	0.11	0.1556	0.1905
Cut depth (mm)	0.1344	0.19	0.2687	0.3291

Table 3 - Equivalent cut depths, major and minor axes for different aspect ratios

The figures below (Fig.8, 9, 10, 11) are a demonstration for all aspect ratios modelled.

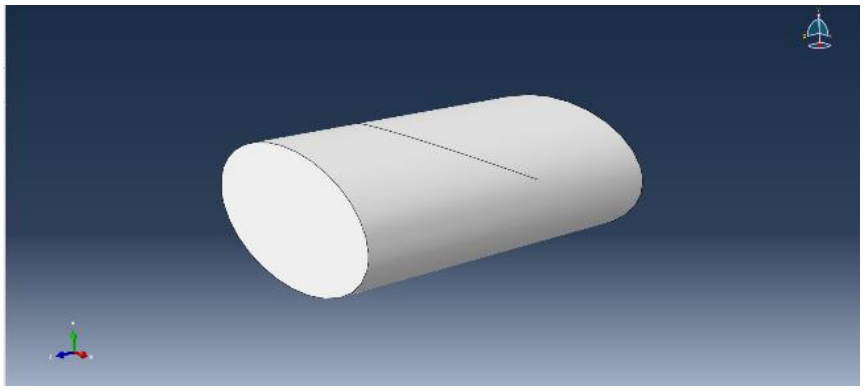

Figure 8 – ρ = ½

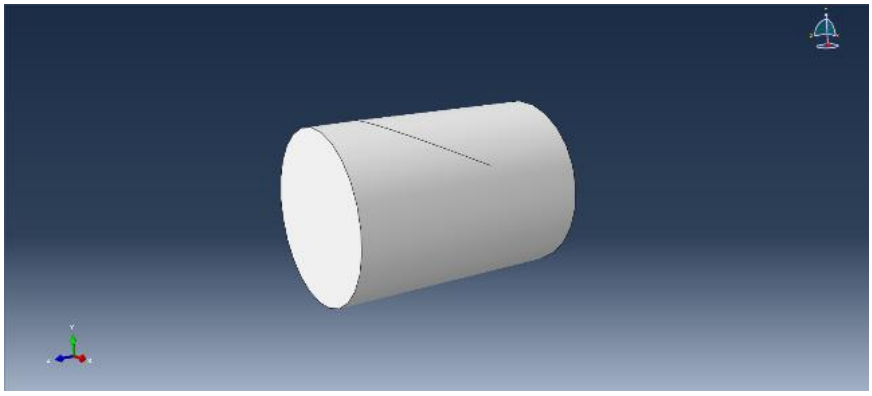

Figure 9 - ρ = 1

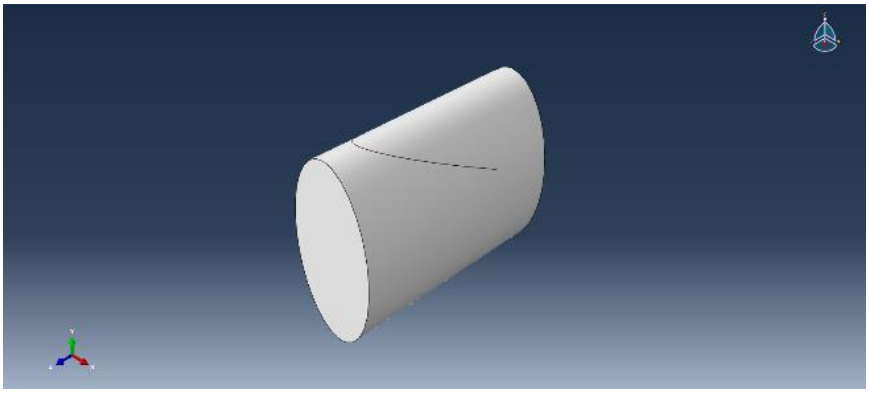

Figure 10 - ρ = 2

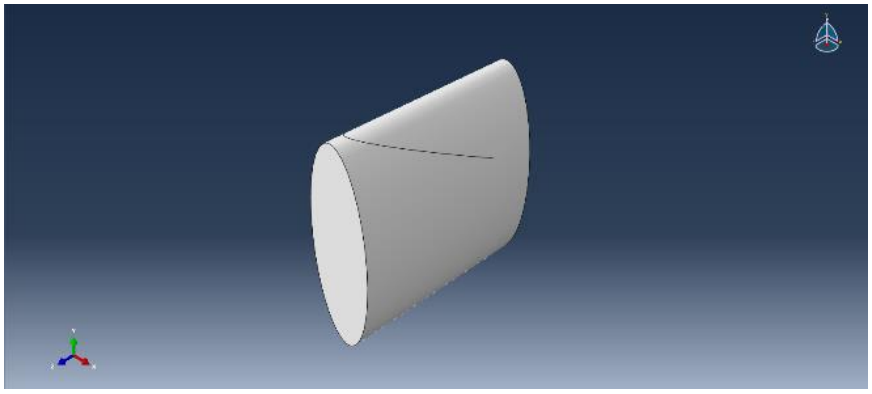

Figure 11 - ρ = 3

After attaining the configuration with the highest strength, an optimization process for the tendon-suture interaction was applied on different cut angles (154°, 160°) and cut depths (0.19, 0.12, and 0.07 mm).

4.2. Material

The material module required the definition of elastic and viscoelastic behaviors. A damage initiation criterion was also needed for the study of crack propagation.

Young's modulus and Poisson's ratio are the two elastic mechanical properties. As discussed earlier, these two parameters were found from tensile experiments:

$E = 1668.67\ MPa$

$\vartheta = 0.36878$

The normalized shear data extracted from experiments was implemented in the viscoelastic shear test data. Abaqus evaluates the material property and generates a curve fit for the stress relaxation data and prony series coefficients. The graph below shows the viscoelastic evaluation of the suture.

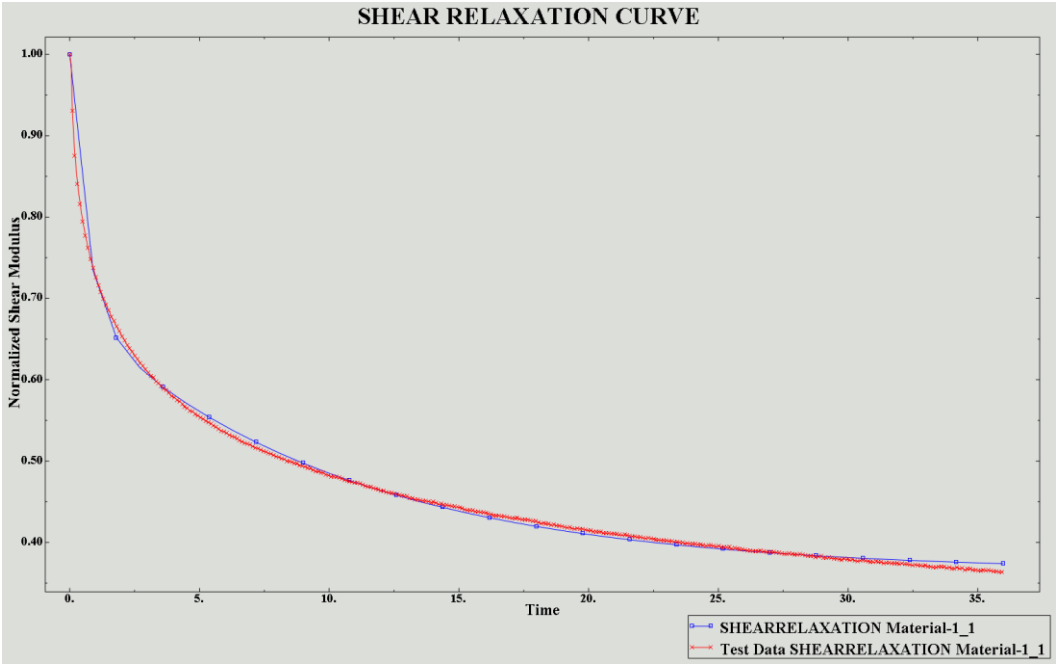

Figure 12 – Curve fit of stress relaxation data

Finally, crack initiation in Abaqus requires a damage initiation criterion. The criterion used is the maximum principal stress, MAXPS.

The maximum principal stress is the true ultimate stress given by:

$$\sigma_t = \sigma_e(1 + \varepsilon_e) \qquad eq.31$$

Where σ_e is the engineering ultimate stress and ε_e the strain at break attained from the experimental stress strain curve (Fig.13).

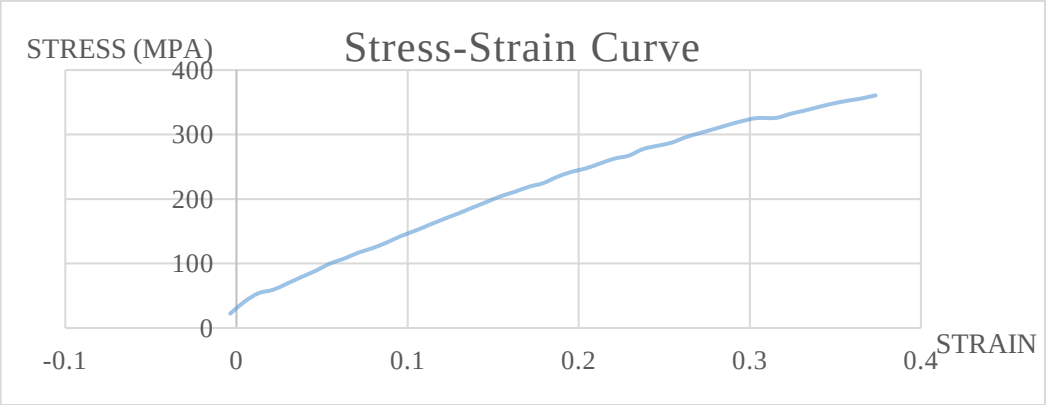

Figure 13 – Stress-Strain curve

$Ultimate\ engineering\ stress = \sigma_e = 353.147\ MPa$

$Strain\ at\ break = \varepsilon_e = 0.39145$

Therefore, $\sigma_t = 353.147(1 + 0.39145) = 491.39\ MPa$

The critical fracture energy release rates for modes I, II, and III are needed for the damage evolution of the material. Fracture toughness properties of polypropylene were studied under compact tension shear specimens [40].

It was found that $K_{IIC} = 0.44\ K_{IC}$, $K_{IIC} = K_{IIIC}$, and the powers of modes I, II, and III are 1, 2, 1 respectively.

The graph below shows the values of the critical stress intensities for modes I and II.

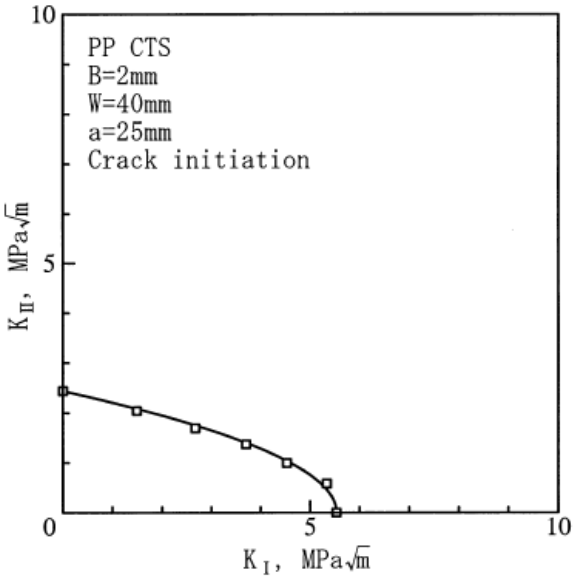

Figure 14 – Polypropylene stress intensities for Modes I and II [40]

$K_{IC} = 5.5\ MPa.m^{1/2}$

$K_{IIC} = 2.42\ MPa.m^{1/2}$

For plane strain conditions, K and G are related by equation 10. Therefore,

$$G_{IC} = \frac{5.5^2\ (1 - 0.36878^2)}{1668.67} = 0.015663\ MPa.m = 15.663\ MPa.mm$$

$$G_{IIC} = \frac{2.42^2\ (1 - 0.36878^2)}{1668.67} = 3.0323\ MPa.mm = G_{IIIC}$$

The inputted values for the damage evolution criterion are tabulated below:

Normal Mode Fracture Energy	Shear Mode Fracture Energy First Direction	Shear Mode Fracture Energy Second Direction
15.663	3.0323	3.0323

Table 4 – Modes I, II, and III fracture energy

4.3. Step [28]

To simulate the fatigue loading condition of the suture, a direct cyclic step was used for modelling. The classical approach for obtaining the stabilized cyclic response of a structure is to use a combination of Fourier series and time integration of its nonlinear material behavior iteratively. The direct cyclic analysis allows for the direct calculation of the cyclic response of the suture. By that, the numerical expense associated with a transient analysis is avoided. The response of the suture at all times, t, during a load cycle having a period, T, is described by a displacement function, $u(t)$.

This step is a quasi-static analysis. It can be used for linear and nonlinear materials having localized plastic deformation and to forecast plastic ratchetting. The direct cyclic step does not account for geometric nonlinearities and assumes fixed contact conditions. In order for the equation system to be inverted once, the elastic stiffness is used. This step predicts the progressive damage and failure of the material by using the low cycle fatigue analysis.

To attain solution accuracy, the material history and residual vector must be calculated at an adequate number of time points, n_T, during the cycle. For the integration of residual coefficients, Abaqus uses a trapezoidal rule that is based on the linear variation of the residual over time. The response is computed at a number of time points greater than the number of Fourier coefficients.

$$n_T > 2n + 1 \qquad eq.32$$

The number of Fourier terms is dependent on the variation of the load and structural response over the period. Since this step uses low cycle fatigue analysis, the local inaccuracies in stresses are disregarded. However, the target is to get a noble

approximation of the plastic strain cycle at each point. An accurate solution is obtained by an increasing the number of Fourier terms, but this costs extra computational time. If the number of Fourier coefficients used in the next iteration is greater than the number of increments taken to complete an iteration, Abaqus automatically moderates the number.

Convergence is defined by small residual vector coefficients and corrections to displacement coefficients in the Fourier series. By default, the initial term used for studying the response of the structure iteratively is 11. Abaqus takes this value and checks if equilibrium at all time points during a cycle is satisfied. If so, the number of Fourier coefficients is sufficient and the solution is accepted. Else, the number of terms is increased by the increment size and the iterative method is repeated until the maximum number of Fourier terms leads to convergence. The outline below is a demonstration where local equilibrium and overall convergence are obtained for a specific number of Fourier terms.

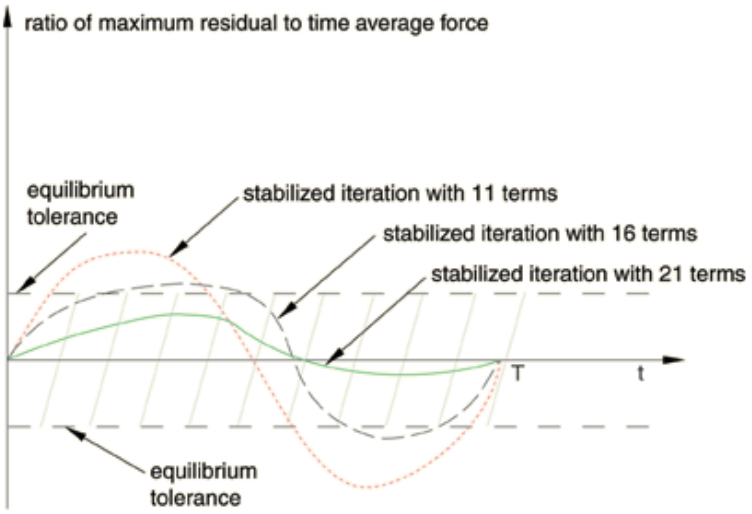

Figure 15 – Stabilization of Fourier coefficients [28]

In the basic-tabbed page of this step, the cycle time period, T, must be determined. In the incrementation-tabbed page, the maximum number of increments allowed for a time period, the maximum number of iterations for a single cycle, the fixed increment size, and the Fourier coefficients must be implemented.

The initial and maximum numbers of Fourier terms were set to 11 and 25 respectively with increments of 5. In order to obtain the fixed increment size given by $ncrement\ size = \frac{T}{n_T} \quad eq.33$, the following procedure was followed:

$2n + 1 = 2(11) + 1 = 23$

Considering equation 32, assume that $n_T = 25 > 23$.

Therefore, $increment\ size = \frac{1}{25} = 0.04$

In the fatigue-tabbed page, the low cycle fatigue analysis must be toggled. This type of analysis uses the direct cyclic step to study the stabilized response of the structure under periodic loading. The cycle increment size represents the number of cycles at the previously mentioned fixed increment size over which damage is extrapolated. The minimum and maximum cycle increment size, ΔN_{min} and ΔN_{max} were set to 50 and 100 respectively. For instance, if the suture fractures at a cycle lower than 50, the analysis will enter the cycle of fracture and iterate until the convergence of the solution. Nevertheless, if it lives for 100 cycles, the analysis will jump with increments of 50 until it reaches the total number of cycles, 100.

The user can determine the total number of cycles, N, needed to study the response of the structure. Therefore, the deduced total time of the analysis is:

$$Total\ \ Time\ (\text{sec}) = N \times T \quad eq.34$$

Early active mobilization prevents tissue adhesion and results in a faster healing process. Hence, flexor tendons require a rehabilitation program that accounts for approximately 10000 cycles when the suture is still effective [41].

Stage I

- Early active movement 3-5 days post-op
- 3 repetitions every 2 hours

Therefore,

- Passive motion for 5 fingers ➔ $5 \times 3 \times 10 = 150$ rep/day
- Active motion for 5 fingers ➔ $5 \times 3 \times 10 = 150$ rep/day
- Active motion entirely ➔ $3 \times 10 = 30$ rep/day

Stage II begins after 4 weeks (28 days). Then, the total number of cycles predicted for the therapy of flexor tendons was calculated as such:

$N = (150 + 150 + 30) \times (28 - 3) = 8250$ cycles

Low cycle fatigue analysis accounts for $N \leq 10^4$ [42]. Initially, N was set to 100. If the suture did not fracture at 100 cycles, this number was reset to 10000 to confirm its infinite life.

The table below summarizes all the values entered in the direct cyclic step.

Cycle time period	1 sec
Maximum number of increments	10000
Increment size	0.04
Maximum number of iterations	10
Initial number of Fourier terms	11
Maximum number of Fourier terms	25
Fourier increment size	5
Minimum cycle increment size	50
Maximum cycle increment size	100
Number of cycles	100

Table 5 - Direct cyclic step parameters

4.4. Interaction

The interaction module was used to create a crack and define a fracture criterion. The body of the suture and the barb represented the crack domain and the crack location respectively. The type of crack and its interaction property were defined. XFEM crack type that ensures an arbitrary propagation was selected. The interaction property included the previously mentioned VCCT fracture criterion.

In the definition of this criterion, the maximum tangential stress determined the direction of crack growth relative to local 1-direction. Moreover, Power law was selected as the mixed mode behavior. The values of the critical energy release rates for the three modes along with the powers were mentioned previously.

These values were implemented again in the VCCT fracture criterion as shown in the table below:

G_{IC}	G_{IIC}	G_{IIIC}	a_m	a_n	a_o
15.663	3.0323	3.0323	1	2	1

Table 6 - VCCT fracture criterion

The suture is intrinsically flawed. In this scenario, the crack propagation study is based on the principles of LEFM used in Paris law (eq.11).

The figure below shows the result of polyethylene fatigue crack propagation [36].

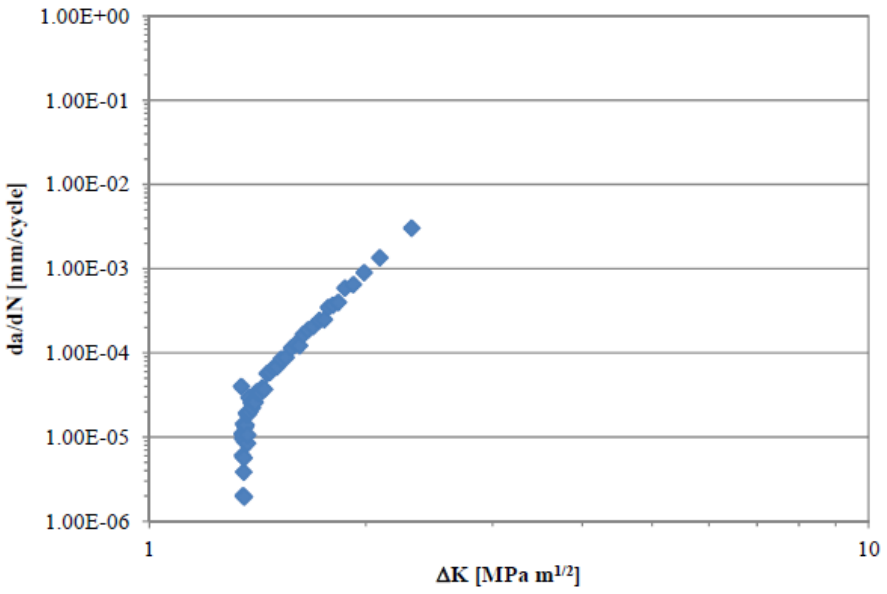

Figure 16 - FCP of polyethylene [36]

After applying a linear regression to this curve, the values of C and n are:

$$C = 1.9 \times 10^{-6} \frac{mm}{cycle(MPa\sqrt{m})^m} = 6 \times 10^{-20} \frac{mm}{cycle(MPa\sqrt{mm})^m}$$

$$n = 9$$

Paris law implemented in Abaqus is represented by the critical energy release rates (eq.23) and therefore considers c_3 and c_4 the two fitting fatigue parameters. Since the stress intensity and the energy release rate are related (eq.10), then substituting equation 10 with equations 11 and 23 gives the conversion of Paris law coefficients used in the low cycle fatigue analysis [43]:

$$c_4 = \frac{m}{2} \qquad \text{eq.}35$$

$$c_3 = C(E')^{c_4} \qquad eq.36$$

As a result:

$$c_4 = \frac{9}{2} = 4.5$$

$$c_3 = 6 \times 10^{-20}(\frac{1668.67}{1 - 0.36878^2})^{4.5} = 3.67 \times 10^{-5}$$

Paris law was implemented in the keywords of Abaqus by replacing the generated VCCT fracture criterion with the following data lines.

**Fracture Criterion, type=Fatigue, mixed mode behavior=POWER, normal direction=MTS, viscosity=1e-05*

, , c_3, c_4, r_1, r_2, G_{IC}, G_{IIC}

G_{IIIC}, a_m, a_n, a_0

Where, $r_1 = \frac{\Delta G_{th}}{\Delta G_C}$ and $r_2 = \frac{\Delta G_{pl}}{\Delta G_C}$

From the Paris regime curve obtained from FCP:

$\Delta K_{th} = 1.35\ MPa\sqrt{m}$

$\Delta K_{pl} = 2.5\ MPa\sqrt{m}$

$\Delta K_C = 2.9\ MPa\sqrt{m}$

From equation 10:

$\Delta G_{th} = 0.94\ MPa.mm$

$\Delta G_{pl} = 3.23\ MPa.mm$

$\Delta G_C = 4.35\ MPa.mm$

Therefore, $r_1 = 0.216$ and $r_2 = 0.743$.

The data lines below demonstrate the Paris law implementation in Abaqus.

**Fracture Criterion, type=Fatigue, mixed mode behavior=POWER, normal direction=MTS, viscosity=1e-05*

, , 3.67×10^{-5}, 4.5, *0.216, 0.743, 15.663, 3.0323*

3.0323, *1*, 2, 1

4.5. Boundary Conditions and Loading

For the four aspect ratios stated earlier in the geometry module, the strength of the suture and the strength of the barb were of high interest. Load case 1 represented the strength of the suture and load case 2 that of the barb. For each case, the same loading condition was applied to the four aspect ratios to reach the best configuration.

In a cyclic analysis, the load must be assigned to an amplitude that shows the variation of this load with time. The amplitude curve in this study was defined by a tabular method. This method is represented by a table of values at convenient points on the time scale. Since the step time was set to 1 second for all models, the table below summarizes the amplitude used for all loading conditions.

Time span = Step time	
Time/Frequency	**Amplitude**
0	0
0.5	1
1	0

Table 7 - Amplitude definition

Consequently, the load will reach its maximum value at 0.5 sec and then return to zero (i.e. initial state) at 1 sec.

4.5.1. Suture Strength

To study the tensile strength of the suture, two boundary conditions were applied on the surfaces of the geometry. The boundary conditions were created in the initial step and then propagated to the direct cyclic step. The type selected was Displacement/Rotation. The first condition was applied on the surface of one edge with zero displacement and rotation in all directions (U1, U2, U3, UR1, UR2, UR3 = 0). The second condition was applied on the opposite surface with a displacement only in the z

direction, U3, and zero displacement and rotation in all other directions. The amplitude tabulated above was assigned to these displacements.

The figure below illustrates the first loading condition:

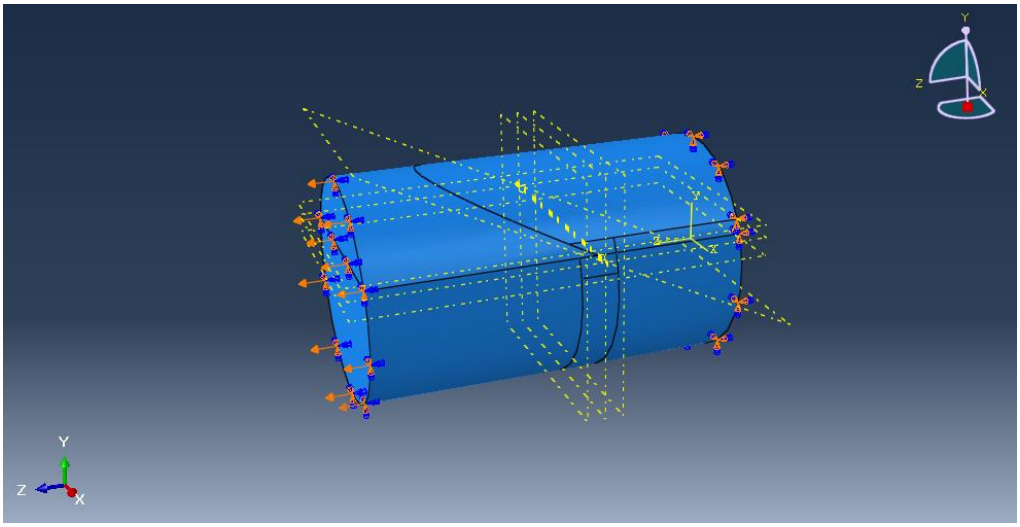

Figure 17 - Suture strength

4.5.2. Barb Strength

To study the strength of the barb, two fixed boundary conditions were applied on the surfaces of the edges and a load was applied on the barb. The boundary conditions were created in the initial step and then propagated to the direct cyclic step. The type selected was Encastre (U1, U2, U3, UR1, UR2, UR3 = 0).

A plane parallel to the plane of the crack was created in order to apply the force on the barb. The application of a concentrated force requires a nodal set. Hence, a set was created in the new plane in the assembly module.

The load was created immediately in the direct cyclic step. Concentrated force was the type selected with uniform distribution. The direction of the force was perpendicular to the plane of the barb. Therefore, the force had y and z components (CF2 and CF3) and zero x component (CF1). The same amplitude was assigned to the force application.

The following equations were used to calculate CF2 and CF3 respectively:

$$CF2 = \frac{Force\ magnitude\ \times \sin 64}{number\ of\ nodes} \qquad eq.37$$

$$CF3 = -\frac{Force\ magnitude\ \times \cos 64}{number\ of\ nodes} \qquad eq.38$$

The figure below illustrates the second loading condition:

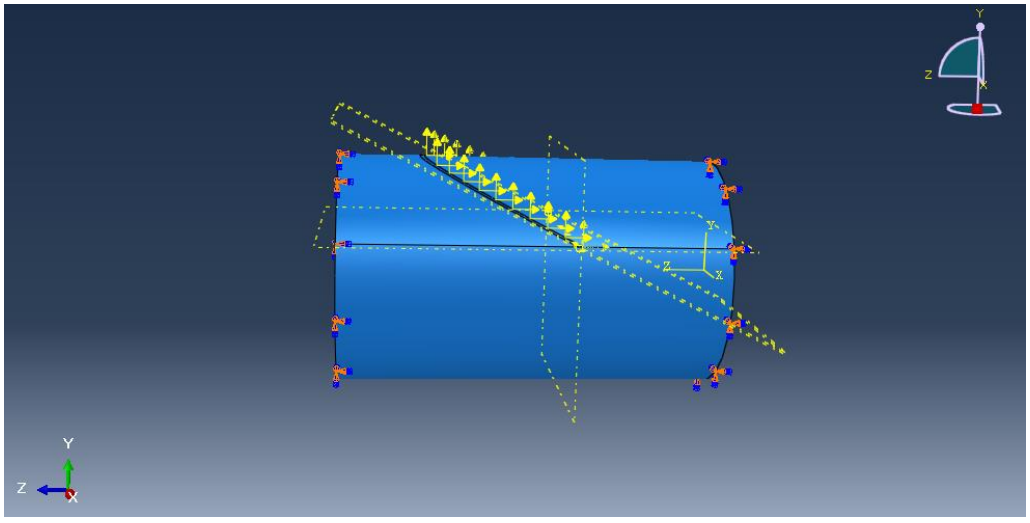

Figure 18 - Barb strength

Finally, after finding the aspect ratio with the highest suture and barb strengths, a tendon-suture interaction model was generated. The best aspect ratio obtained was

optimized for two cut angles (154° and 160°) and three cut depths (0.19, 0.12, and 0.07 mm). The optimization process was studied under the third loading condition.

4.5.3. Tendon-Suture Interaction

To study the real life application of the suture in the tendon, the barb and the suture were subjected to forces. Records for tendon forces were found for different wrist positions [44]:

- Place and hold
- Active finger flexion
- Isolated FDP flexion
- Isolated FDS flexion
- Tenodesis

The isolated FDP flexion when the wrist is in neutral position has the highest mean force value (25 Newton). Hence, for safe design measures, the tendon force applied on the suture was found by:

$$F = 25 \times 1.6\ (safety\ factor) = 40\ Newton$$

Therefore, the suture was fixed from one end and subjected to this magnitude from the other end. The control in this study is the number of barbs needed to withstand 40 Newton. So, a concentrated force was applied also on the barb and varied until an optimum value was found.

A fixed boundary conditions was applied on the surface of one edge. The boundary condition was created in the initial step and then propagated to the direct cyclic step. The type selected was Encastre (U1, U2, U3, UR1, UR2, UR3 = 0).

A plane parallel to the plane of the crack was created in order to apply the force on the barb. The application of a concentrated force requires a nodal set. Hence, a set was created in the new plane and on the plane of the edge.

Two loads were created immediately in the direct cyclic step. Concentrated force was the type selected with uniform distribution. For the first load, the direction of the force was perpendicular to the plane of the barb. Therefore, the force had y and z components (CF2 and CF3) and zero x component (CF1). The same amplitude was assigned to this force application.

The following equations were used to calculate CF2 and CF3 respectively:

$$CF2 = \frac{Force\ magnitude\ \times \sin(cut\ angle - 90)}{number\ of\ nodes\ for\ corresponding\ set} \qquad eq.39$$

$$CF3 = -\frac{Force\ magnitude\ \times \cos(cut\ angle - 90)}{number\ of\ nodes\ for\ corresponding\ set} \qquad eq.40$$

For the second load, the direction of the force was in the positive z direction. Thus,

$CF1 = 0$, $CF2 = 0$, and $CF3 = \frac{40}{number\ of\ nodes\ for\ corresponding\ set}$

The figure below illustrates the tendon-suture interaction loading condition:

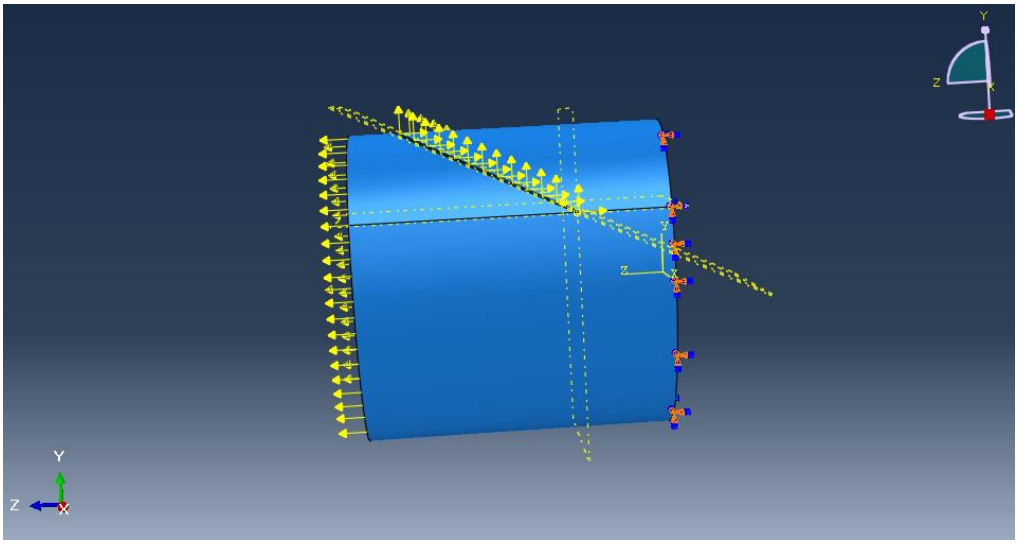

Figure 19 - Tendon-suture interaction

4.6. Mesh

Mesh sensitivity study was conducted on the circular geometry, $\rho = 1$, having cut depth 0.19 mm and cut angle 154° for the two loading conditions mentioned above. For the first condition, mesh convergence was studied under a static load. That helped by proving that the strain at break was equivalent to the experimental one. As for the second condition, a mesh study was made by changing the global mesh size for the circular geometry and checking the magnitude of the force that the barb can withstand.

4.6.1. Load case 1

At the beginning, a hexahedral mesh of C3D8R type was applied on the geometry. However, this type of mesh confronted many problems due to the complication of the geometry at the crack tip. The lower body of the geometry was meshed, but the elements at the crack tip and the surface of the crack were not capable to be meshed. Therefore, a tetrahedral mesh of type C3D4 was applied on the geometry

(Fig.20). The seeding size was global and the structure was easily meshed as an instance. The curve (Fig.21) shows that there was a fluctuation in the results for meshes with 85062 and 60375 elements.

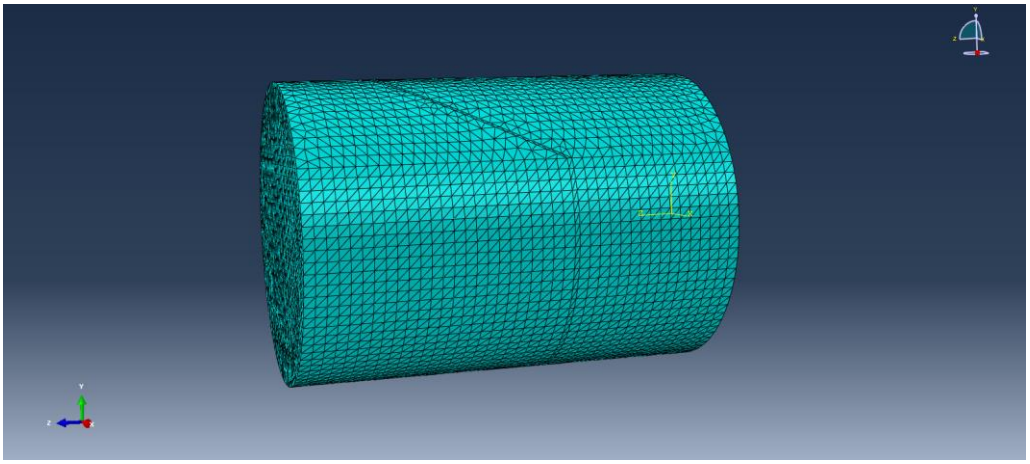

Figure 20 - Tetrahedral mesh

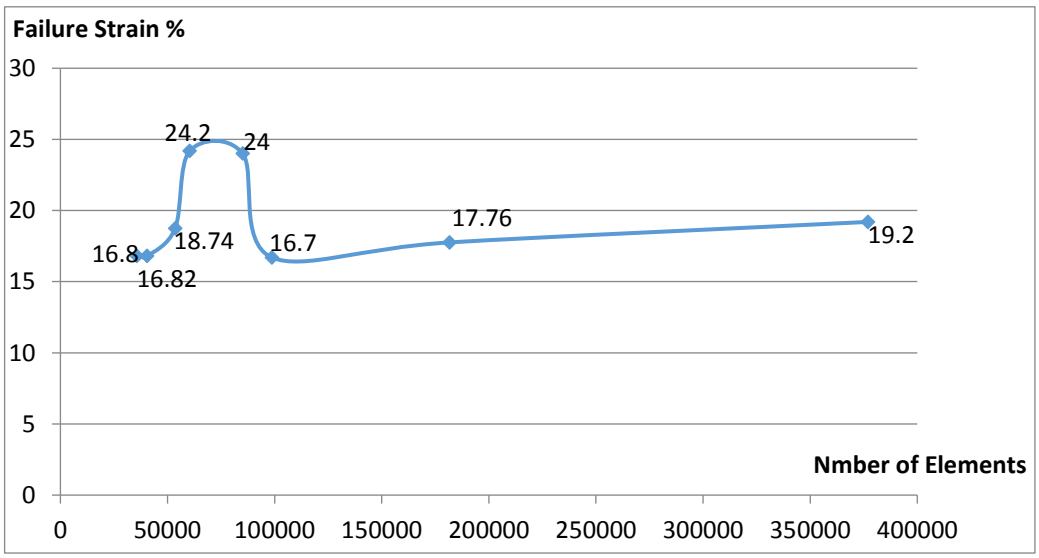

Figure 21 - Mesh sensitivity for tetrahedral elements

To resolve the issue of convergence, a tetrahedral mesh of size 0.025 was applied on the whole structure and a structured hexahedral mesh on the region near the

crack tip (Fig.22). Different mesh sizes on the structured region were studied. The graph below (Fig.23) shows that mesh convergence was met. The element size selected for the study was 0.025 with 124261 elements.

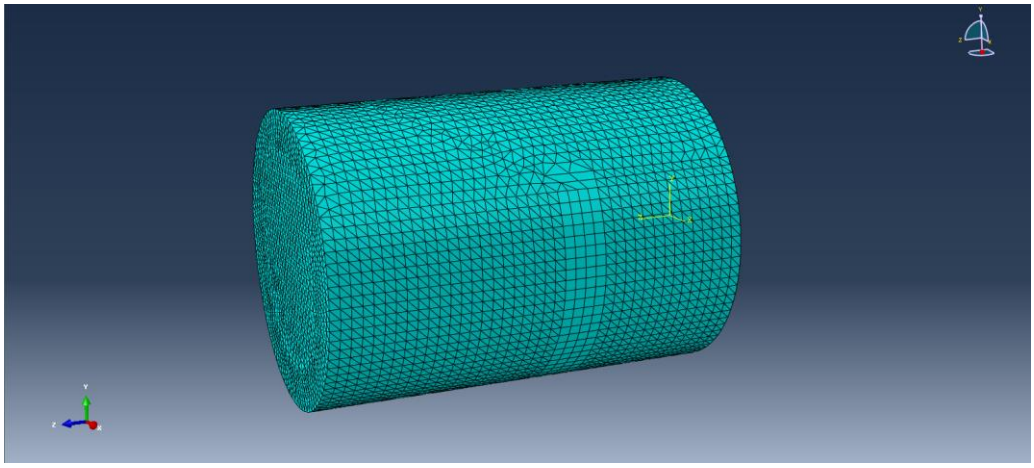

Figure 22 - Hexahedral structured mesh near the crack tip

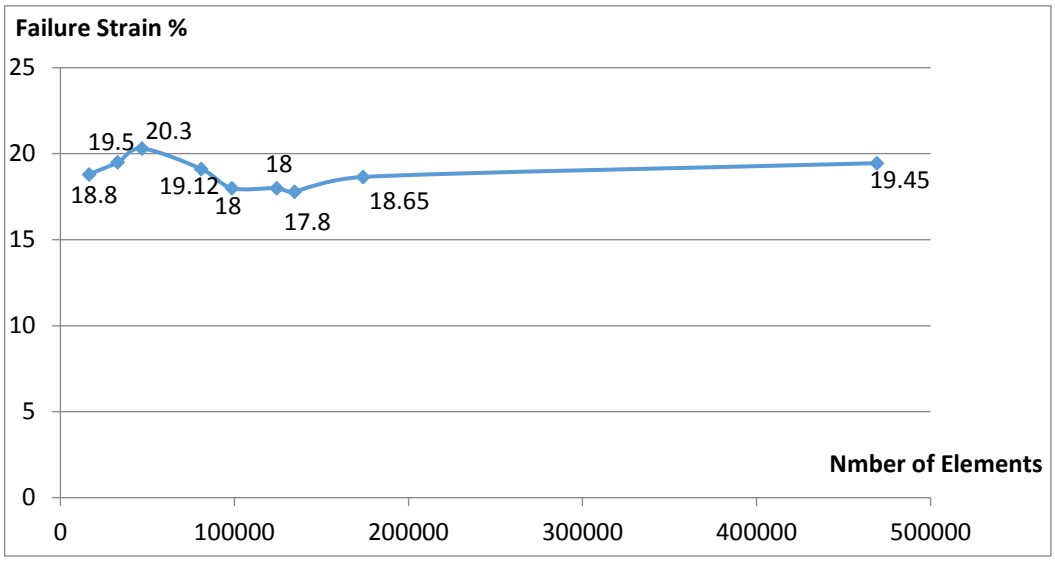

Figure 23 - Mesh convergence of structured elements

4.6.2. Load case 2

For a force-controlled study, the structured mesh was not applicable. Upon running the analysis for different force magnitudes, no crack propagation was realized. Thus, the mesh type used for load case 2 and the tendon-suture interaction condition was C3D4. The table below shows that the force magnitude a barb can withstand does not vary much with the variation of mesh size. So, the finest mesh of size 0.025 was selected.

Mesh size	Threshold Force (Newton)
0.025	6
0.03	5
0.035	5

Table 8 - Mesh convergence of force-controlled model

CHAPTER 5

RESULTS

For all loading conditions, the purpose is to find the configuration that can tolerate the highest displacement or force. Since, the number of cycles required for the rehabilitation of the tendon is ≈ 10000, then infinite life of the suture in the low cycle fatigue analysis corresponds to 10^4 cycles. The results of the three previously mentioned loading conditions are presented below.

5.1. Suture Strength

	Z direction displacement, U3 (mm)	
	0.09	**0.1**
$\boldsymbol{\rho = \frac{1}{2}}$	Infinite life	Crack propagation after 8 cycles
$\boldsymbol{\rho = 1}$	Infinite life	Crack propagation after 8 cycles
$\boldsymbol{\rho = 2}$	Infinite life	Crack propagation after 13 cycles
$\boldsymbol{\rho = 3}$	Infinite life	Crack propagation after 15 cycles

Table 9 - Results of Load Case 1 - Crack initiation

Since all geometries endured the same displacement, 0.09 mm, to 10000 cycles, then the comparison will be based on the number of cycles required to initiate a

crack for U3 = 0.1 mm. It should be noted that once a crack is initiated and fracture occurs, this give significance to a weak suture; but the aim is to choose the best configuration. Hence, the aspect ratio with highest number of cycles needed to initiate a crack will be considered the ultimate one. For the same displacement, 0.1 mm, $\rho = 3$ required the maximum number of cycles to initiation, which is 16 cycles. In order to compare results having the same number of cycles needed to initiate a crack ($\rho = \frac{1}{2}\ and\ \rho = 1$) , a displacement of 0.5 mm was applied on all aspect ratios and the total number of cycles to failure was recorded (Fig.24). From the bar graph, the total number of cycles to failure for $= \frac{1}{2}$, 15 cycles, was found to be less than that of $\rho = 1$, 21 cycles. Hence, the graph below validates that the geometry with $\rho = 3$ is the most durable with highest number of cycles to initiation and failure.

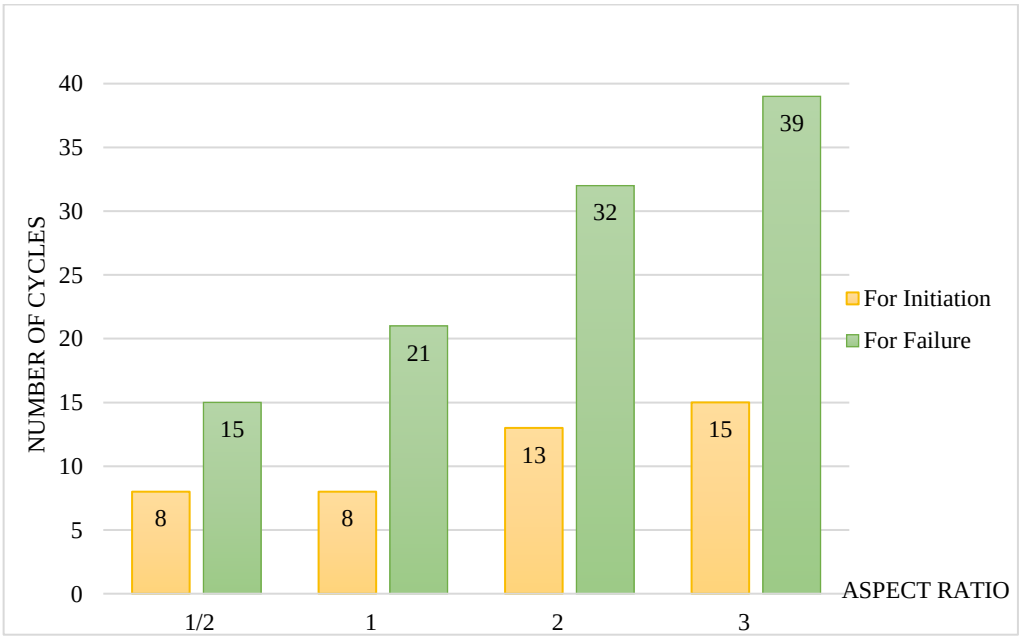

Figure 24 - Results of Load Case 1 - Number of cycles for crack Initiation & failure

The illustration below shows an ascending order of the geometry's strength.

$$\rho = \frac{1}{2} < \rho = 1 < \rho = 2 < \rho = 3$$

The figure below is an illustration of the failure mechanism under the first loading condition.

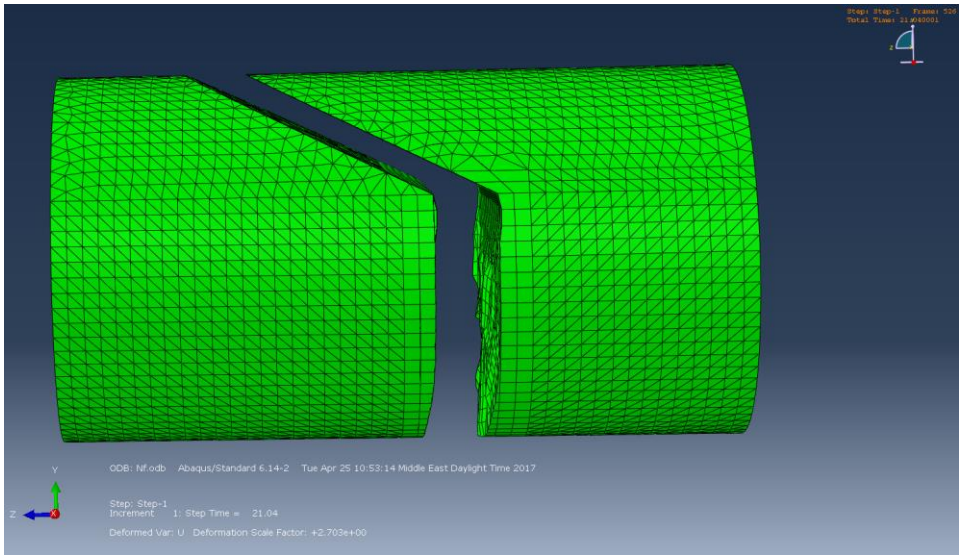

Figure 25 - Suture strength failure mechanism

5.2. Barb Strength

For the second loading condition, sutures with $\rho = 2$ and $\rho = 3$ resisted the highest yet same magnitude of force applied on the barb. For these two ratios, the crack was initiated at a force of 10 N applied on the barb. As for $\rho = \frac{1}{2}$ and $\rho = 1$, fracture begins at 4 N and 7 N respectively. Consequently, sutures with $\rho = \frac{1}{2}$ and $\rho = 1$ are much weaker than those with $\rho = 2$ and $\rho = 3$. In order to compare the latter

geometries, the number of cycles required to initiate the crack was considered. One cycle initiated a crack for $\rho = 2$ and two cycles for $\rho = 3$.

	Force at which a crack propagates
$\boldsymbol{\rho = \frac{1}{2}}$	4 N
$\boldsymbol{\rho = 1}$	7 N
$\boldsymbol{\rho = 2}$	10 N
$\boldsymbol{\rho = 3}$	10 N

Table 10 – Results of Load Case 2

The same order of the geometry's strength as load case 1 was obtained.

$$\rho = \frac{1}{2} < \rho = 1 < \rho = 2 < \rho = 3$$

The figure below is an illustration of the peeling failure mechanism under the second loading condition.

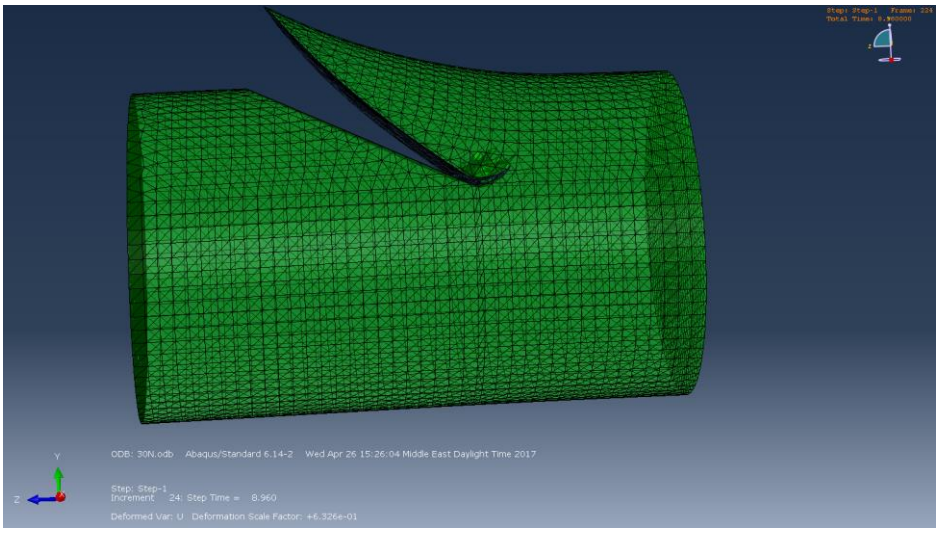

Figure 26 - Barb strength failure mechanism

5.3. Optimization

After finding that the best geometry for both loading conditions has an aspect ratio = 3, the tendon cross sectional area was considered. The results of flexor tendons' aspect ratios were mentioned previously and close to 2. Hence, for the safety of the design, the suture was optimized according to the aspect ratio of FDS of finger 5, $\rho = 1.75$ (Table 2).

Hence, $\rho = 2$ which is close to 1.75 was taken as the best configuration obtained from load case 1 and 2. The values of a and b for finger 5 FDS were considered. The assumed dimensions for the new geometry were $a = 0.5\ mm$ and $b = 0.25\ mm$., The previously mentioned procedure (4.1.) was applied in order to get the equivalent cut depths. The table below summarizes the results.

	$\boldsymbol{\rho = 1}$	$\boldsymbol{\rho = 2}$
Major Axis (a, mm)	0.3536	0.5
Minor Axis (b, mm)	0.3536	0.25
Cut Depth (mm)	0.07	0.099
	0.12	0.1697
	0.19	0.2687

Table 11 - Ellipse equivalence for the optimized geometry

In this study, the tendon force is known. However, the control is the number of barbs needed to endure this force. Therefore, for the suture-tendon interaction

optimization stage, the load applied on the body of the suture, as discussed in load case 3, was set to 40 N. The force applied on the barb was set to 1 N as an initial condition for all the models. The results are tabulated below.

	Cut angle	
Cut depth	154°	160°
0.19 mm	No crack propagation	Propagation after 1 cycle
0.12 mm	No crack propagation	Propagation after 1 cycle
0.07 mm	Propagation after 2 cycles	Propagation after 1 cycle

Table 12 - Results for the optimized configurations

After noticing that the configurations of cut angle 154°, cut depth 0.19 mm and cut angle 154°, cut depth 0.12 mm did not initiate a crack growth, the load on the barb was increased to 2 N for these two arrangements. Both models featured a crack propagation. However, the number of cycles needed to initiate the crack for cut depth 0.19 mm was 4 and that for 0.12 mm was 1. The barb that can hold the maximum load with the force being applied on the suture will correspond to the ideal design.

Accordingly, the recommended geometry of the suture with aspect ratio 2 ($\rho = \frac{0.5}{0.25}$) is the one that has a cut angle = 154° and cut depth = 0.19 mm (Fig.27).

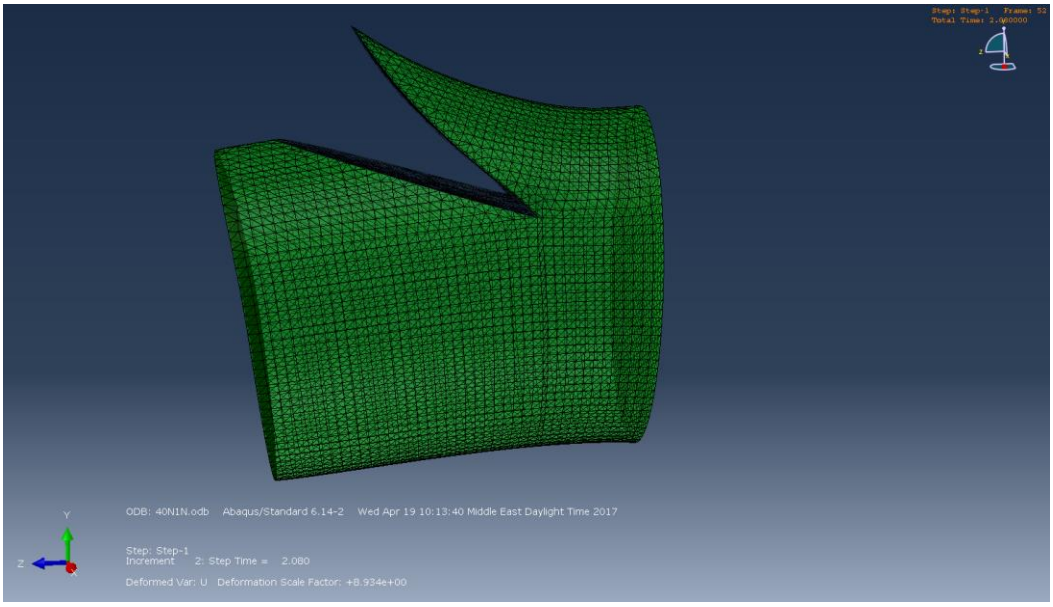

Figure 27 – Geometry of the optimized design of a barbed suture

This model was simulated on the closest barb to the application of the force. This makes the design a safer one, especially that the barbs away from this load will not feel the same effect as the one modelled. In the optimal configuration model, the barb tolerated 1 Newton for 10000 cycles. Thus, assuming that the barbs will equally feel the tendon force, the total number of barbs needed for a fatigue loading study is around 40 barbs.

CHAPTER 6

DISCUSSION OF RESULTS

For load case 1 and 2, the cut angle and cut depth were fixed and the only variable was the aspect ratio. Varying the aspect ratios gives different crack sizes, c.

$c_{\rho=1/2} > c_{\rho=1} > c_{\rho=2} > c_{\rho=3}$ (Figs.28, 29, 30, 31)

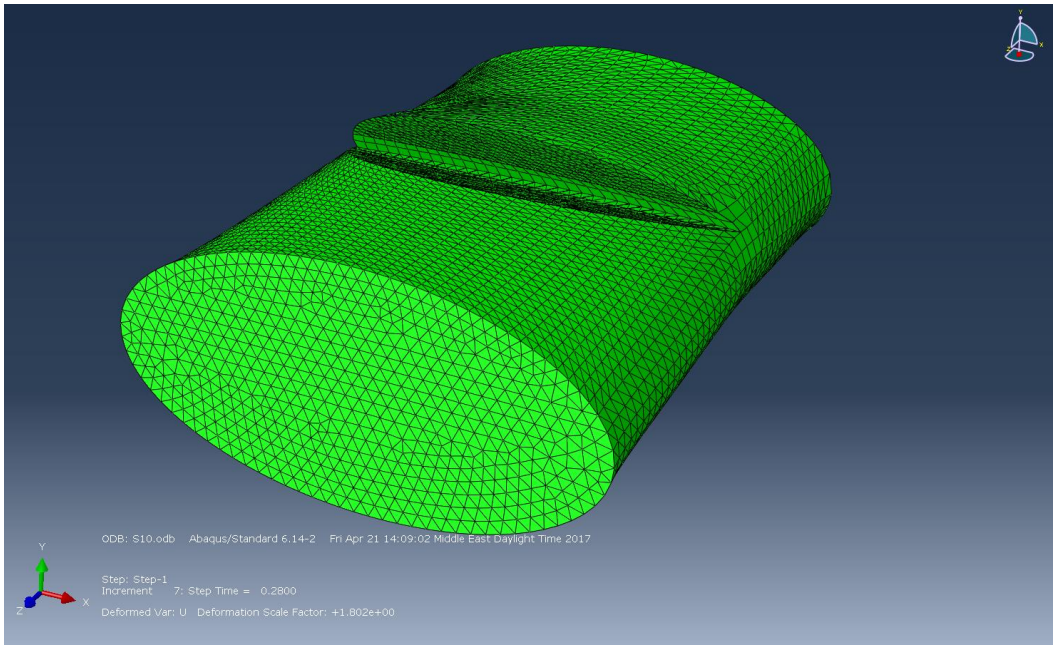

Figure 28 - Crack size for $\rho = 1/2$

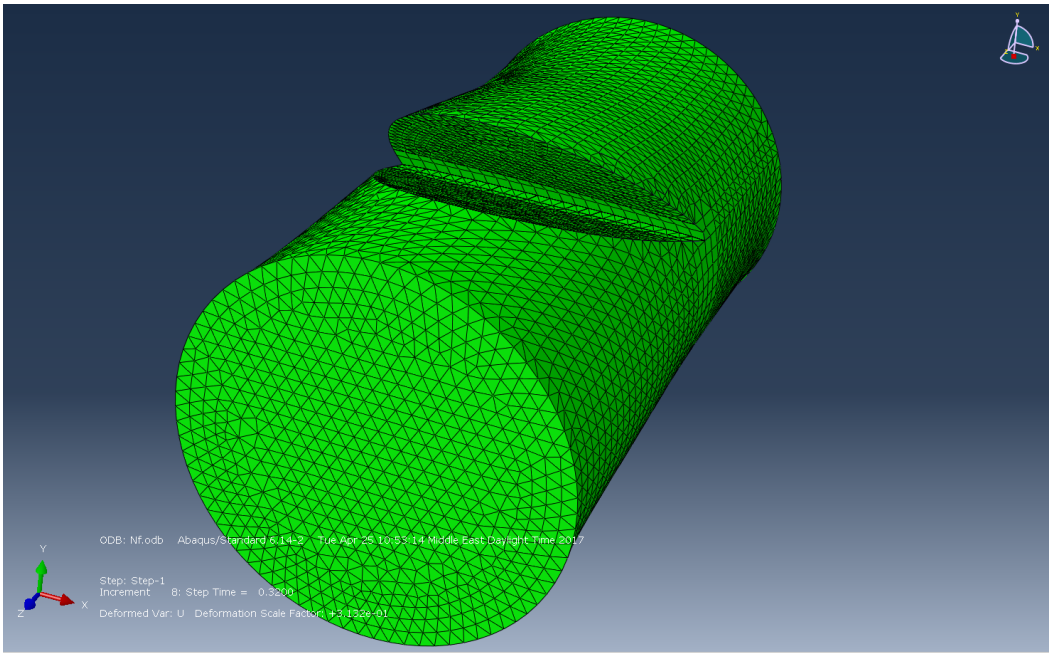

Figure 29 - Crack size for ρ = 1

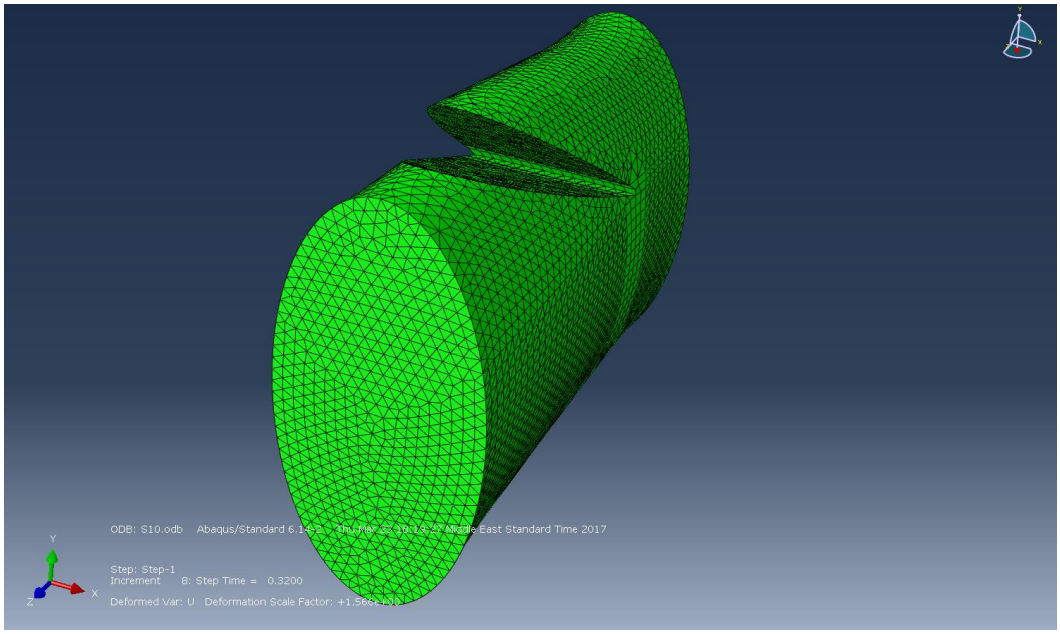

Figure 30 - Crack size for ρ = 2

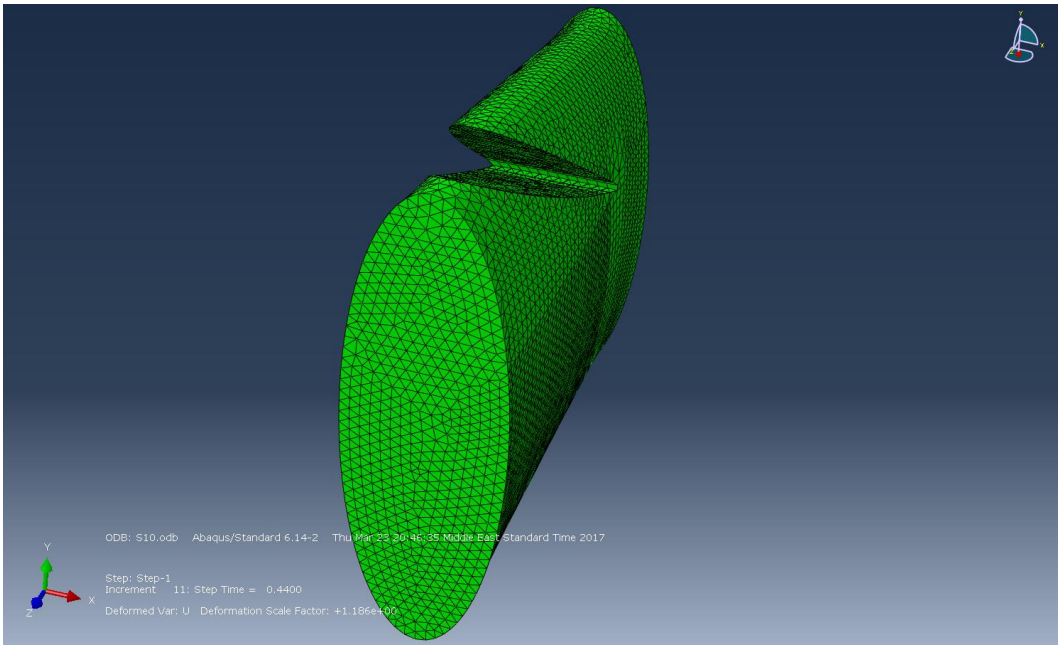

Figure 31 - Crack size for ρ = 3

As the crack size decreases, the stress intensity decreases as well [45] and this direct proportionality is depicted earlier (eq.8). Knowing that the stress intensity is directly related to the energy release rate (eq.10), then for smaller crack sizes G is smaller. Therefore, the model with aspect ratio 3 has the smallest crack size and thus the lowest energy release rate. This corresponds to the highest number of cycles needed to initiate crack propagation (15) and highest number of cycles for complete fracture (39) for load case 1. Similarly, for load case 2, the threshold force for crack propagation was the highest for geometries with $\rho = 2, 3$ (10 N) and $\rho = 3$ required more number of cycles for crack initiation.

In the optimization process, the aspect ratio was fixed ($\rho = 2$) and the variables were the cut depth and cut angle. For a constant cut depth, as the cut angle increases, the remaining area decreases and therefore the suture becomes weaker. For a

constant cut angle, the larger the cut depth, the higher the barb area. According to the equation below:

$$\sigma = \frac{F}{A}$$

For a fixed force, the stresses are reduced and therefore for higher cut depths more number of cycles are needed for crack initiation. The results obtained in table 12 validate the discussion.

CHAPTER 7

CONCLUSION AND FUTURE WORK

7.1. Conclusion

Sutures used for flexor tendon repair were studied under fatigue loading conditions. Experimentally informed extended finite element analysis in Abaqus was performed to study the crack propagation of sutures. The strength of the suture and that of the barb were represented by two loading conditions. Sutures with aspect ratio 3 gave the highest strength. Inspired by the tendon elliptical cross sectional area, the model with aspect ratio 2 was considered for optimization. Two cut angles (154° and 160°) and three cut depths (0.19, 0.12, and 0.07 mm) were demonstrated to get the best configuration. For the same aspect ratio, fixing the cut depth while increasing the cut angle results in a weaker suture. And, fixing the cut angle while increasing the cut depth results in a stronger suture. The best suture geometry under cyclic loading was found to be: $\rho = 2$, cut angle = 154°, cut depth = 0.19 mm.

7.2. Future Work

- Consider a suture material that has superior mechanical properties compared to polypropylene.
- Study temperature effects on the performance of the suture.
- Perform an experimental validation for the optimized geometry reached.
- Calculate the number of barbs required to be anchored in the tendon taking into consideration that not all barbs will carry the same load.

REFERENCES

1. Vizesi, F., et al., *Stress relaxation and creep: viscoelastic properties of common suture materials used for flexor tendon repair.* The Journal of hand surgery, 2008. **33**(2): p. 241-246.
2. Shah, A., M. Rowlands, and A. Au, *Barbed Sutures and Tendon Repair—a Review.* HAND, 2015. **10**(1): p. 6-15.
3. Strickland, J.W., *Development of flexor tendon surgery: twenty-five years of progress.* The Journal of hand surgery, 2000. **25**(2): p. 214-235.
4. McClellan, W.T., et al., *A knotless flexor tendon repair technique using a bidirectional barbed suture: an ex vivo comparison of three methods.* Plastic and reconstructive surgery, 2011. **128**(4): p. 322e-327e.
5. Jordan, M.C., et al., *Suture material for flexor tendon repair: 3-0 V-Loc versus 3-0 Stratafix in a biomechanical comparison ex vivo.* Journal of orthopaedic surgery and research, 2014. **9**(1): p. 1.
6. Hantouche, M.M., *Flexor tendon repair using sutures with different cross sectional areas*. 2013.
7. Trail, I., E. Powell, and J. Noble, *An evaluation of suture materials used in tendon surgery.* Journal of Hand Surgery (British and European Volume), 1989. **14**(4): p. 422-427.
8. Greenwald, D., et al., *Mechanical comparison of 10 suture materials before and after in vivo incubation.* Journal of surgical research, 1994. **56**(4): p. 372-377.
9. Naleway, S.E., et al., *Mechanical properties of suture materials in general and cutaneous surgery.* Journal of Biomedical Materials Research Part B: Applied Biomaterials, 2015. **103**(4): p. 735-742.
10. Dennis, C., et al., *Suture materials—Current and emerging trends.* Journal of Biomedical Materials Research Part A, 2016. **104**(6): p. 1544-1559.
11. Ingle, N.P., *Mechanical Performance and Finite Element Analysis of Bi-directional Barbed Sutures.* 2004.
12. Lin, T.E., et al., *Biomechanical analysis of knotless flexor tendon repair using large-diameter unidirection barbed suture.* Hand, 2013. **8**(3): p. 315-319.
13. Vijayakumar, A., P. Murdeshwar, and H. Sanghvi, *Barbed Suture in Tendon Repair.* Journal of Advanced Plastic Surgery Research, 2015. **1**: p. 5-9.
14. Ingle, N. and M. King, *Optimizing the tissue anchoring performance of barbed sutures in skin and tendon tissues.* Journal of biomechanics, 2010. **43**(2): p. 302-309.
15. Parikh, P.M., S.P. Davison, and J.P. Higgins, *Barbed suture tenorrhaphy: an ex vivo biomechanical analysis.* Plastic and reconstructive surgery, 2009. **124**(5): p. 1551-1558.
16. Kanz, B.N., et al., *Biomechanical evaluation of a knotless barbed suture repair in a human Achilles tendon rupture model.* Foot & ankle specialist, 2014. **7**(3): p. 176-181.
17. Marrero-Amadeo, I.C., et al., *Flexor tendon repair with a knotless barbed suture: a comparative biomechanical study.* The Journal of hand surgery, 2011. **36**(7): p. 1204-1208.
18. Ingle, N., M. King, and M. Zikry, *Finite element analysis of barbed sutures in skin and tendon tissues.* Journal of biomechanics, 2010. **43**(5): p. 879-886.
19. Ingle, N.P., *Prototyping and Finite Element Analysis of Tissue Specific Barbed Sutures.* 2009.
20. Vincent, J.F., *Structural biomaterials*. 2012: Princeton University Press.
21. Drabousky, D.P., *Prony series representation and interconversion of viscoelastic material functions of equine cortical bone*. 2009, Case Western Reserve University.
22. Tzikang, C., *Determining a Prony series for a viscoelastic material from time varying strain data.* 2000.

23. Melson, J.H., *Fatigue Crack Growth Analysis with Finite Element Methods and a Monte Carlo Simulation*. 2014, Virginia Tech.
24. Anderson, T.L. and T. Anderson, *Fracture mechanics: fundamentals and applications*. 2005: CRC press.
25. Kurtz, S.M., *UHMWPE biomaterials handbook: ultra high molecular weight polyethylene in total joint replacement and medical devices*. 2009: Academic Press.
26. Pascoe, J., R. Alderliesten, and R. Benedictus, *Methods for the prediction of fatigue delamination growth in composites and adhesive bonds–a critical review.* Engineering Fracture Mechanics, 2013. **112**: p. 72-96.
27. Rans, C. and R. Alderliesten. *Formulating an effective strain energy release rate for a linear elastic fracture mechanics description of delamination growth*. in *Proceedings of 17th international conference on composite materials (ICCM-17)*. 2009.
28. SIMULIA, A., *6.12-1.* ABAQUS Analysis User's Manual, 2011.
29. Brown, D. and M. Cowling, *Numerical simulation of fatigue crack growth.* International journal of fatigue, 1983. **5**(4): p. 199-206.
30. Jensen, B.E.W., *Numerical Analysis of Crack Propagation and Lifetime Estimation.*
31. Carpinteri, A. and M. Paggi, *Are the Paris' law parameters dependent on each other?* Frattura ed Integrità Strutturale, 2007(2): p. 10.
32. Schapery, R., *A theory of crack initiation and growth in viscoelastic media.* International Journal of Fracture, 1975. **11**(1): p. 141-159.
33. Sirimamilla, A., J. Furmanski, and C. Rimnac, *Peak stress intensity factor governs crack propagation velocity in crosslinked ultrahigh- molecular- weight polyethylene.* Journal of Biomedical Materials Research Part B: Applied Biomaterials, 2013. **101**(3): p. 430-435.
34. Ansari, F., et al., *Notch fatigue of ultrahigh molecular weight polyethylene (UHMWPE) used in total joint replacements.* Journal of the mechanical behavior of biomedical materials, 2016. **60**: p. 267-279.
35. Sirimamilla, P.A., J. Furmanski, and C.M. Rimnac, *Application of viscoelastic fracture model and non-uniform crack initiation at clinically relevant notches in crosslinked UHMWPE.* Journal of the mechanical behavior of biomedical materials, 2013. **17**: p. 11-21.
36. Group, C.P., *Fatigue Crack Propagation Experiments*. 2013.
37. Elbert, K., et al., *Fatigue crack propagation behavior of ultra high molecular weight polyethylene under mixed mode conditions.* Journal of Biomedical Materials Research Part A, 1994. **28**(2): p. 181-187.
38. Shrewsbury, M.M. and K. Kuczynski, *Flexor digitorum superficialis tendon in the fingers of the human hand.* The Hand, 1974. **6**(2): p. 121-133.
39. Ward, S.R., et al., *High stiffness of human digital flexor tendons is suited for precise finger positional control.* Journal of neurophysiology, 2006. **96**(5): p. 2815-2818.
40. Saito, Y. and M. Yoda, *Fracture toughness and creep crack growth in polypropylene under combined modes I and II loading.* International journal of fracture, 2004. **127**(2): p. L161-L166.
41. Berger, R.A. and A.-P.C. Weiss, *Hand surgery*. Vol. 1. 2003: Lippincott Williams & Wilkins.
42. Anand, L. and D. Parks, *Defect Free Fatigue.* Massachusetts Institute of Technology Department of Mechanical Engineering Cambridge, Mechanics and Materials II, 2004: p. 1-37.
43. London, T., D. De Bono, and X. Sun. *An Evaluation of the Low Cycle Fatigue Analysis Procedure in Abaqus for Crack Propagation: Numerical Benchmarks and Experimental Validation*. 2015. SIMULIA UK Regional User Meeting.
44. Edsfeldt, S., et al., *In vivo flexor tendon forces generated during different rehabilitation exercises.* Journal of Hand Surgery (European Volume), 2015. **40**(7): p. 705-710.

45. McCarver, J. and R. Ritchie, *Fatigue crack propagation thresholds for long and short cracks in Rene 95 nickel-base superalloy.* Materials Science and Engineering, 1982. **55**(1): p. 63-67.